Final report

1.1 Project details

Project title	Design of next generation wind turbine rotors (NextRotor)
Project identification (program abbrev. and file)	EUDP 2011-I, J.nr.: 64011-0094
Name of the programme which has funded the project	EUDP
Project managing company/institution (name and address)	DTU Wind Energy Nils Koppels Alle, Building 403, 2800 Lyngby
Project partners	DTU Wind Energy, LM Wind Power
CVR (central business register)	30060946, 76490511
Date for submission	

1.2 Short description of project objective and results

English

The aim of the project is the design aerodynamic efficient and low-noise wind turbine blades, thereby making Danish wind turbines blades more competitive in the future world wind energy market. The idea behind the collaboration between the research institution and the blade manufacturer is the development of a reliable integrated rotor design tool and the design of efficient, low noise rotors that are demanded in the future wind energy market.

Results from the project are

- A new low noise airfoil family DTU-LN2xx has been designed and tested in LM's wind tunnel.
- The low noise CQU-DTU-LN118 airfoil has been tested in the acoustic wind tunnel at Virginia Tech.
- A new integrated airfoil and rotor design tool has been developed.
- A new 3D viscous-inviscid code MIRAS has been developed.
- Low noise blades for 3MW and 10MW turbines have been designed.
- Validations using CFD and CAA computations have been carried out for both new airfoils and rotors.

Dansk

Projekts formål er at designe aerodynamisk effektive og støjsvage vindmøllevinger, for hvorved at bidrage til at gøre Danskproducerede vindmøllevinger mere konkurrencedygtige på det globale vindenergimarked. Ideen bag samarbejdet mellem forskningsinstitutionen og producenten af vindmølleblade, er at udvikle et pålideligt integreret designværktøj til rotorer, samt at udforme effektive og støjsvage rotorer, hvilket efterspørges på det fremtidige vindenergimarked.

Resultater fra projektet er

- En ny lavstøj vingeprofilfamilie - DTU-LN2xx - er blevet udviklet og testet i LM's vindtunnel.
- Et støjsvagt vingeprofil - CQU-DTU-LN118 - er blevet testet i den akustiske vindtunnel på Virginia Tech.
- Et nyt integreret vingeprofil- og rotordesign værktøj er blevet udviklet.
- En ny 3D viskos-inviskos kode - MIRAS - er blevet udviklet.
- Støjsvage vinger for 3MW og 10 MW møller er designet.
- CFD og CAA beregninger er udført for både nye vingeprofiler og rotorer.

1.3 Executive summary

The objective of the project is the design of a new type of wind turbine rotors which at the same time has aerodynamically high efficiency, low cost and low noise emission. The project explores the collaboration between the Technical University of Denmark and LM Wind Power Blades on developing new wind technology. The design wind turbine blades require knowledge on aerodynamics, structure dynamics and its mutual interaction of airfoils and rotor blades. The project is divided into four work packages: design of wind turbine airfoils, experimental verification of the designed airfoils, design of wind turbine rotors and CFD validations of the designed airfoils and rotors. The outcome of the project is (1) reliable tools for designing and validating high efficient, low cost and low noise rotors, (2) designed airfoils and rotors to demonstrate the reliability of the design tools. The tools have been demonstrated for design of a series of high performance, low noise wind turbine airfoils and rotors. The aerodynamic and acoustic performance of the airfoils has been validated experimentally.

1.4 Project objectives

The overall objective of the project is to develop and provide new reliable tools for designing and validating highly efficient, low cost and low noise blades/rotors. Wind energy is captured by wind turbines through the rotor blades. A rotor blade is constructed using airfoil sections that originally were used for aircrafts, but which in the later years have been tailor-made to the specific operating conditions of wind turbines. To improve wind turbines' performance while respecting noise regulation, there are basically two important steps: design high efficiency wind turbine airfoils with low noise emission; and design highly efficient wind turbine blades with low noise emission.

Being able to reduce airfoil noise on wind turbine blades without reducing the aerodynamic properties will result in two main achievements: 1) it will allow for more wind turbines to be situated onshore, thus allowing a larger installed capacity and 2) it will allow wind turbines to run with increased tip speed. The tip speed of the blades on the rotor is directly governed by noise considerations. If airfoil noise can be reduced, it is possible to run at higher tip speeds, which potentially can either increase the rotor speed or increase the size of the rotor. In both cases, annual energy yield will increase, leading to a reduction in overall cost of energy. When running at higher rotor speed (keeping the power constant), the magnitude of the torque going through the drive train is reduced, leading to better reliability and lower cost of the drive train system.

The project evolved as foreseen and accordingly to the milestones agreed upon. A new family of high performance and low noise airfoil family (DTU-LN218, DTU-LN221, DTU-LN224, DTU-230, and DTU-236) have been designed according to the requirements provided by LM and tested in the LM wind tunnel. The previously designed wind turbine airfoil CQU-DTU-LN118 has been tested in the acoustic wind tunnel located in Virginia Tech, USA. Advanced rotor design tools including the 3D viscous-inviscid MIRAS code and the integrated airfoil and rotor design code have been developed. New efficient and low noise wind turbine blades for 3MW and 10MW rotors have been designed and compared with the reference NM80 wind turbine equipped with LM 38.8 blades.

There were mainly two risks associated with the project. The first risk was the experimental validation of the aero-acoustic features of the designed airfoil CQU-DTU-LN118 in Virgina Tech. If the experimental result would not be expected, the project had to be stopped. The other risk was the renovation from the LM LSWT wind tunnel into a noise measurement facility. After a feasibility study about the background noise, it turned out that background noise is much louder than noise generated by an airfoil. Due to this fact, the two milestones related to the renovation of the wind tunnel have been modified to those on robust measurement devices. The second risk is also a not expected problem that the project experienced.

As LM is a wind turbine blade manufacturer and also a partner of the present EUDP project, the process to the final market is shortened. For marketing of the technology, LM integrates the developed design tool into its current design and production processes.

1.5 Project results and dissemination of results

In this section, the main results from the NextRotor project are described. It comprises new low noise airfoil design, wind tunnel tests, low noise rotor design, CFD validations, and commercial results.

1.5.1 Design of the low noise airfoil family DTU-LN2xx

The low noise airfoil family DTU-LN2xx (DTU-LN218, DTU-LN221, DTU-LN224) is designed using the same design method as for the CQU-DTU-LN1xx airfoils but with LM's requirements and constraints. The principles of the design method can be found in Cheng et al. [1]. The design requirements and constraints are summarized as follows:

- Minimizing maximum lift
- Minimizing roughness sensitivity
- Improving after stall conditions
- Improving structural properties
- Maximizing design lift and design lift-drag ratio

From the requirements listed above, it is seen that some requirements are contradicting with other requirements.

Using the design method with the mentioned requirements, 3 new airfoils of the airfoil family DTU-LN2xx are designed. The shape of the airfoils is plotted in Figure 1.

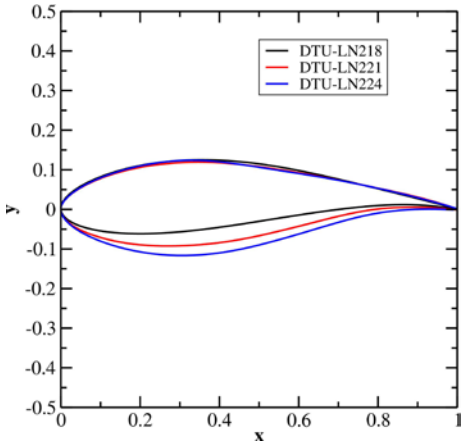

Figure 1: DTU-LN218, DTU-LN221 and DTU-LN224 airfoils

Table 1: Aerodynamic performance of the DTU-LN2xx airfoils

	Clmax Free/force	Cl/Cd Free/force	Cl at 7°	ΔClmax	δ* force suction
LN218	1.91/1.89	168/99	1.47/1.40	0.015	0.017
LN221	1.74/1.73	148/92	1.29/1.22	0.012	0.018
LN224	1.59/1.58	148/85	1.19/1.11	0.014	0.018

Table 2: Aerodynamic performance of the DTU-LN1xx airfoils

	Clmax Free/force	Cl/Cd Free/force	Cl at 7°	ΔClmax	δ* force suction
LN118	2.06/2.03	161/103	1.41/1.37	0.03	0.012
LN121	1.87/1.80	169/88	1.40/1.32	0.065	0.019
LN124	1.94/1.71	164/76	1.40/1.26	0.228	0.031

The aerodynamic performances of the new airfoils are listed in Table 1. As compared to the CQU-DTU-LN1xx airfoils in Table 2, it is seen that the roughness sensitivity is better, the after stall performance is better, and the other performances are similar but with much better structural properties.

The DTU-230 and DTU-236 airfoils are designed with a method using shape perturbation function. This method is based on adding smooth perturbations to an initial airfoil. The smooth perturbations Δy are a linear combination of base functions P_k as

$$\Delta y(i)=\sum_{k=1}^{N}\delta_k P_k(i)$$

Base functions can be chosen to be any set of smooth functions [2]. This study is based on the work of [3]. The airfoil is split to an upper and a lower side with leading edge and trailing edge points fixed at x = 0 and x = 1 and the corresponding perturbation functions can be written for the upper surface as

$$\Delta y_u(i)=\sum_{k=1}^{N}\delta_{ku} P_{ku}(i)$$

and for the lower surface as

$$\Delta y_l(i)=\sum_{k=1}^{N}\delta_{kl} P_{kl}(i)$$

The shape functions for upper and lower surface along the x-coordinate are

$$P_{ku}(i)=\sin^{\xi}\left(\pi x_u(k,i)^{g(k)}\right)$$

and

$$P_{kl}(i)=\sin^{\eta}\left(\pi x_l(k,i)^{g(k)}\right)$$

The subscripts *u* and *l* symbolize the upper and lower surface of the airfoil, *k* is the index of the shape modes and *i* is the index of x and y coordinates. Variable *g* corresponds to the maximum location of the base function. This variable is defined by the designer and gives more influence on the decision-making process. The optimization objective is to maximize lift coefficient and lift to drag ratio. The objective function is expressed as

$$obj = \min(\frac{1}{C_p}), C_p = f\left(C_L, \frac{L}{D}\right)$$

The coefficients C_L and L/D are weighted for clean and rough conditions with more emphasis on the rough case. For more information about the design method, the reader is referred to [4].

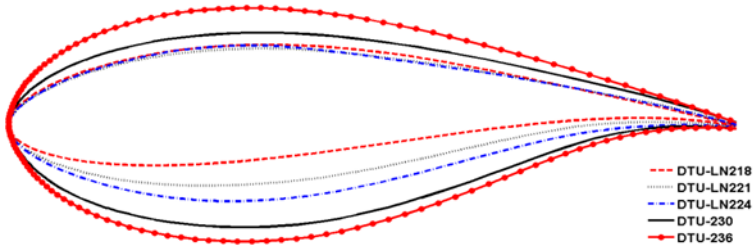

Figure 2: DTU-230 and DTU-236 airfoils

The new DTU-230 and DTU-236 airfoils are plotted in Figure 2. From the figure, it is seen they are geometrical compatible with the LN2xx airfoils.

The experimental verifications of the designed airfoils are given in Section 1.5.3.

1.5.2 Experimental validation of the CQU-DTU-LN118 airfoil

To test the aerodynamic and aero-acoustic features of the CQU-DTU-LN118 airfoil, we performed wind tunnel tests in the stability wind tunnel located at Virginia Tech, USA. The acoustic test section and anechoic chambers are shown in Figure 3 where Kevlar windows between the test section and the chambers are used. The 117 microphones in the microphone array are arranged in a 9-armed spiral of 13 microphones with spacing evaluated using a proprietary AVEC array design code. For more information, the reader is referred to [5].

The airfoil model has a chord length of 0.6 m and a span of 1.82 m. It was made from a full aluminium block by RIVAL A/S in Denmark. The airfoil model was equipped with 62 pressure ports (0.5 mm pinhole diameter). To measure the drag, a wake rake pressure technique was used. Inflow turbulence intensity in the aerodynamic test section measured to be less than 0.05%.

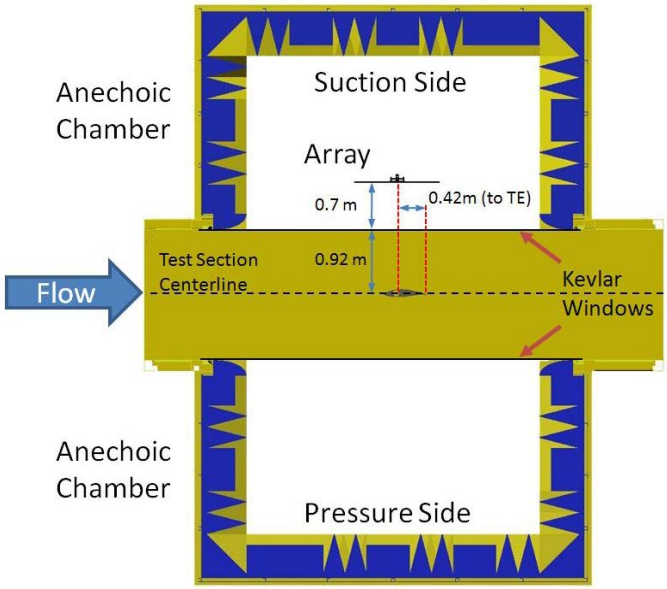

Figure 3: Schematic test section and 117-channel array position in relation to airfoil

The acoustic raw data obtained from the microphone measurement were processed with frequency domain beam-forming technique which can extract the sound pressure level of the trailing edge source from the background noise. The time series was measured with a sampling frequency of 51200Hz during a period of 32 seconds and divided into 200 blocks of 8192 samples to compute the averaged cross spectral density matrix. The beam-forming algorithm proposed in [6] was used, which is different to classical beam-forming in two points:

- The diagonal of the cross spectral density matrix is removed.
- Refraction affects due to the flow in the wind tunnel test section are accounted for by a ray tracing method.

In the experiment of the CQU-DTU-LN118 airfoil made at Virginia Tech, 19 runs were performed at 3 different wind speeds of 30, 45 and 60 m/s which correspond to 3 different Reynolds numbers and 3 different Mach numbers. The first 9 runs were performed with surface pressure taps and far-field microphones whereas the other 10 runs were performed with surface pressure taps and wake rake.

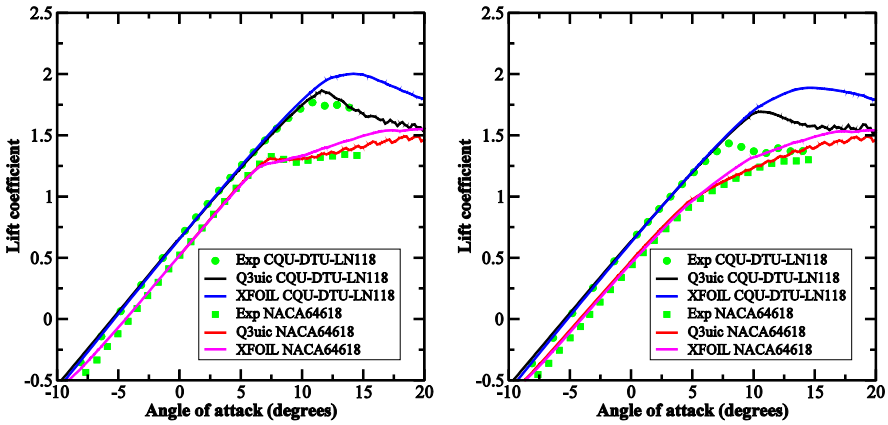

Figure 4: Lift coefficient for flows past a clean (left) and tripped (right) CQU-DTU-LN118 and NACA64618 airfoil at Re=1.6x10^6

To illustrate the high performance of the CQU-DTU-LN118 airfoil, we choose a NACA64618 airfoil which is used in modern wind turbine blades. Another reason is that this airfoil has been tested in the same wind tunnel. Figure 4 shows lift coefficient for both airfoils with both clean and rough surface at a Reynolds number of 1.6x10^6. In the clean case, it is seen that the LN118 airfoil performs better with a higher design Cl and max Cl while in the rough case the differences between the two airfoils are smaller. It is worth noting that both XFOIL and Q^{3}UIC codes predict very well the performance of the NACA airfoil.

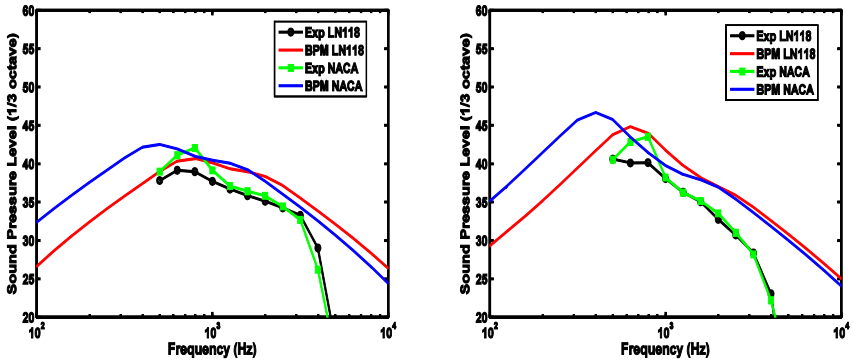

Figure 5: Sound pressure level in 1/3 octave of noise at a distance of 1.62 m and 90^o generated from a CQU-DTU-LN118 airfoil and from a NACA64618 airfoil at a wind speed of 30 m/s and Cl= 0.52 (left) and 0.95 (right)

The aero-acoustic measurements of the CQU-DTU-LN118 airfoil at Virginia Tech were made by AVEC, Inc. Three wind speeds of 30 m/s, 45 m/s and 60 m/s were considered. The clean LN118 airfoil was measured at all the three considered wind speeds while the tripped LN118 airfoil was measured at 45 m/s in order to see the effect of wall roughness on noise emission. To check the low noise design of the CQU-DTU-LN118 airfoil, we compare its noise emission with that of a NACA64618 airfoil which was tested in the same wind tunnel in 2011. Since the two airfoils have different zero-lift angle of attack and stall angle of attack, it is difficult to make a fair comparison about their noise emission at same angle of attack. As airfoil's Cl and Cl/Cd characteristics are the main features when constructing wind turbine blades, we adopt here to compare their noise features at same Cl.

To illustrate, the sound pressure level calculated at a reference point of 1.62 m and 90^o for flows past the CQU-DTU-LN118 and NACA64618 airfoils at a wind speed of 30 m/s is shown in Figure 5. At the same lift coefficient of 0.50 (Figure 5(left)), the experimental data show that the LN118 airfoil produces lower noise in the frequency region below 3000 Hz. Similar results are also seen at Cl=0.94 (Figure 5(right)). To validate the noise prediction (BPM) model, the sound pressure level calculated from the BPM model is also plotted in the same figure. From the figure, the BPM model is seen to slightly over-predict the noise emission from both airfoils but the relative differences between the noise levels from the two airfoils are found to be similar for computation and experiment. The main differences between the two airfoils are seen in the frequency region below 500 Hz. Due to the spatial limitation of the phased microphone array in the experiment, these features cannot be validated.

For more information, the reader is referred to [1] [7].

1.5.3 Experimental validation of the DTU-LN2xx airfoils

To check the performance of the newly designed DTU-LN2xx airfoil family, the 5 airfoils (DTU-LN218, LN221, LN224, DTU-230 and DTU-360) were tested in the LM wind tunnel.

The wind tunnel at LM Wind Power is a closed circuit, variable fan speed tunnel, with cooling system to ensure constant flow temperature. The flow quality is very high with turbulence intensity levels around 0.1%. The tunnel has a contraction of 10 to 1 and is equipped with specially designed corner vanes, a honeycomb structure and three fine mesh screens. The width of the test section is 1.35 m and the height is 2.7 m. The model chord length of 0.9 m at the maximum wind speed of 105 m/s gives a chord Reynolds number of $6x10^6$ and a Mach number of M = 0.3. A wake rake system is used to measurement drag.

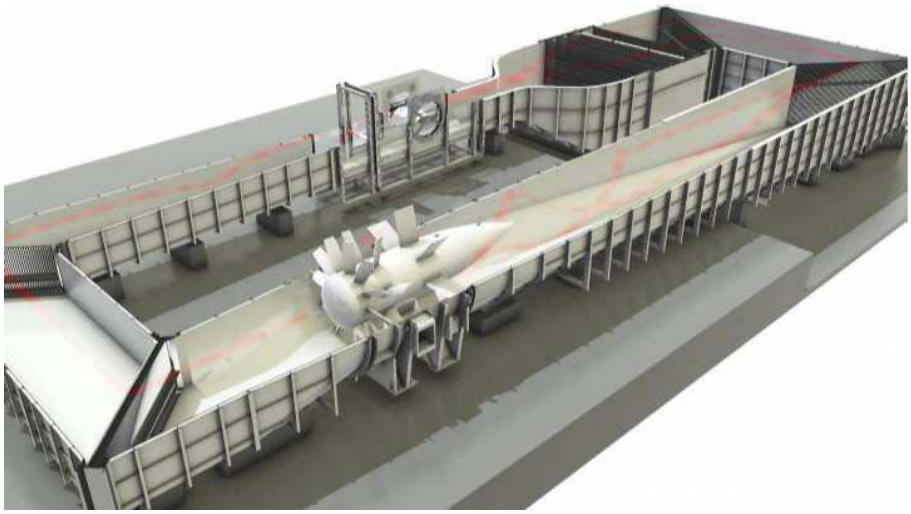

Figure 6: LM low speed wind tuunel

The 5 airfoils were made with a chord of 0.9 m and a span of 1.35 m. On each airfoil model, 64 pressure holes are used to measure the pressure acting on the airfoil. The airfoils were tested at several Reynolds numbers and in different surface configurations with different devices (such as vortex generators and Gurney flaps). The tested Reynolds numbers were Re = 1.5, 3, 4, 5, and $6x10^6$. Airfoil performance in rough conditions was investigated using a standard zig-zag tape and bump tape. Data in rough conditions presented here are measurements with zigzag tape of 0.4 mm thickness placed at 5% chords on the suction side and 10% chords on the pressure side.

To illustrate the performance of the airfoils, selected figures with lift and drag coefficients are shown. In Figure 7, lift coefficient of the DTU-LN218 airfoil is plotted. From the figure, it is seen that most computational codes can predict correctly the lift coefficient until stall for both clean and rough cases. Remark that due to the turbulence level increase in wind tunnel when increasing angle of attack, the max lift is difficult to predict. Comparing the lift performance in clean and rough cases, the roughness sensitivity is very small. The drag coefficient is seen to be well captured by the codes in both clean and rough cases (Figure 8).

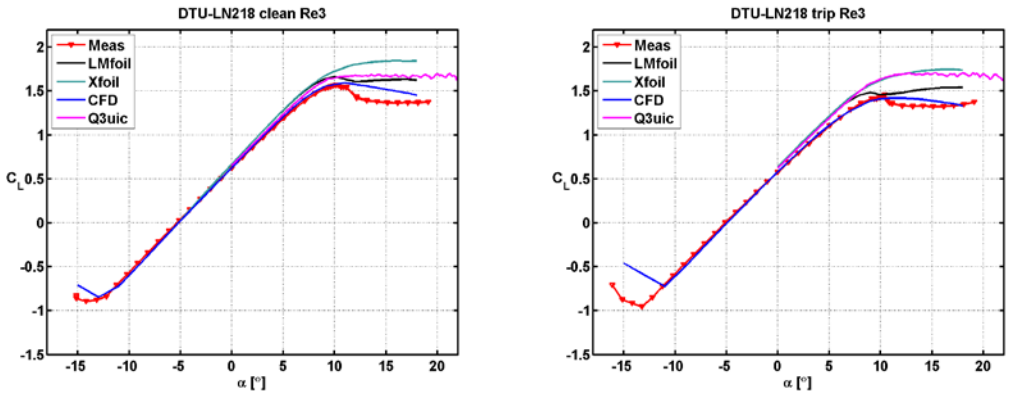

Figure 7: Lift coefficient of the DTU-LN218 airfoil at Re= $3x10^6$ under clean (left) and rough (right) conditions

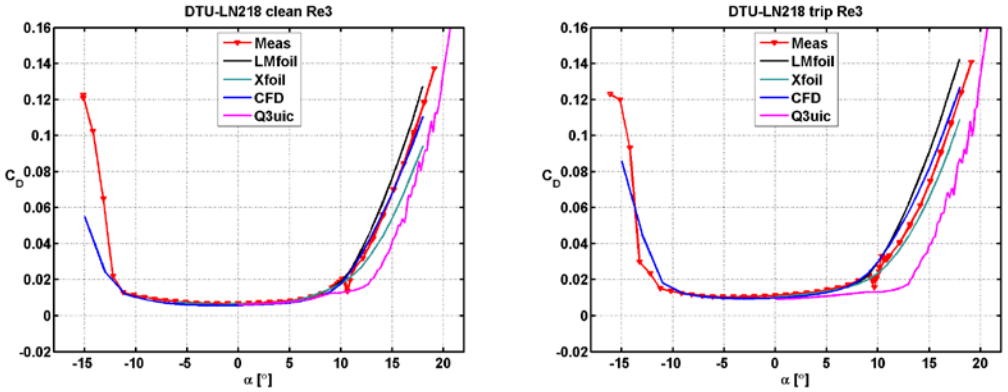

Figure 8: Drag coefficient of the DTU-LN218 airfoil at Re= $3x10^6$ under clean (left) and rough (right) conditions

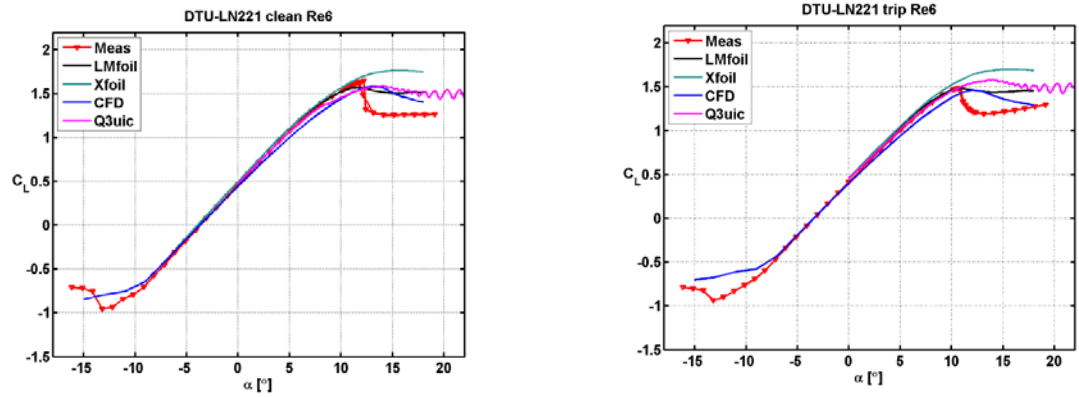

Figure 9: Lift coefficient of the DTU-LN221 airfoil at Re= $6x10^6$ under clean (left) and rough (right) conditions

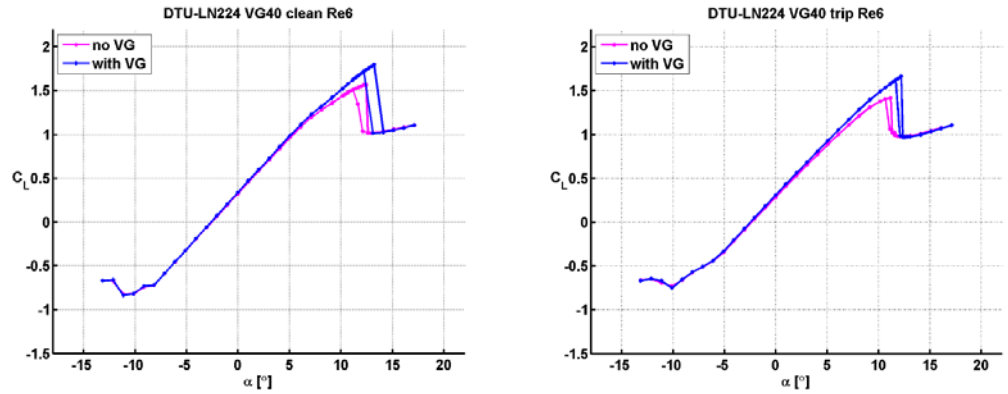

Figure 10: Lift coefficient of the DTU-LN224 airfoil with vortex generator at Re= 6x10^6 under clean (left) and rough (right) conditions

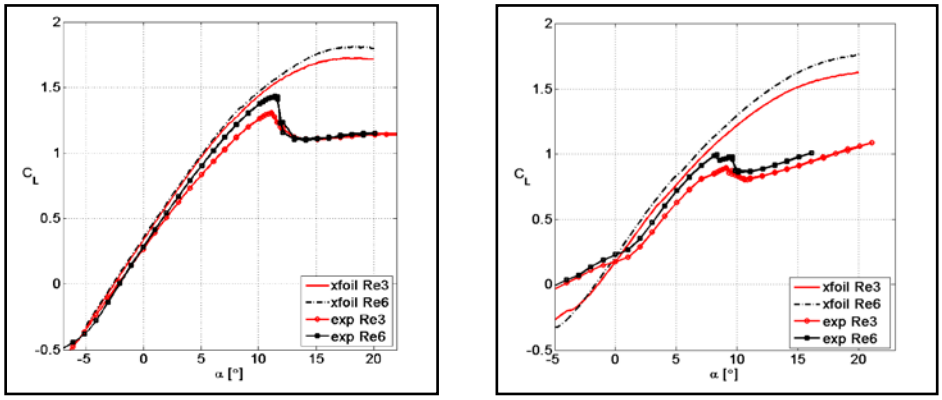

Figure 11: Lift coefficient of the DTU-230 airfoil at Re= 3x10^6 and 6x10^6 under clean (left) and rough (right) conditions

The lift coefficient of the DTU-LN221 airfoil at Re= 6x10^6 in both clean and rough conditions is plotted in Figure 9. Similar behaviours are seen as it is for the DTU-LN218 airfoil. In order to increase airfoil performance, vortex generators are often used on wind turbine blades. Tests were performed with VGs placed in 30% and 40% chords from the leading edge and with Gurney flaps placed at the end of the airfoil. Figure 10 shows the effects of the VGs placed at 40% chords on DTU-LN224. From the figure, the lift coefficient is seen to increase significantly for both clean and rough cases.

Design of thickness airfoils are important. Here the DTU-230 and DTU-236 airfoils presented in Section 1.5.1 were tested in the LM wind tunnel. As an example, lift coefficient of DTU-230 at Re=3x10^6 and 6x10^6 is plotted in both clean and rough conditions. From Figure 11, the performance is seen to be quite well in both conditions. Remark that after stall, the design code XFOIL has some difficulties to capture the lift.

For more details about the measurements, the reader is referred to [8]-[12].

1.5.4 Development of the 3D viscous-inviscid MIRAS code

To fast simulate the flows past wind turbine rotors, the 3D viscous-inviscid interactive code MIRAS has been developed in this project. The principles of the method are summarized here.

Having a potential flow around a solid body with surface S, the velocity at a point in the flow domain, p, can be expressed as a superposition of the undisturbed velocity, $\vec{U}_\infty$, and the disturbance velocity created by the solid body, $\vec{U}_p$,

$$\vec{U}_I = \vec{U}_\infty + \vec{U}_p$$

In the rotating case the undisturbed velocity reads,

$$U_\infty = \sqrt{(\Omega r)^2 + (Q_w)^2} = U_{rel}$$

where r is the spanwise position, Ω is the rotational velocity and Q_w is the wind speed. If the flow is considered to be incompressible, inviscid and irrotational, $\vec{U}_p$ can be expressed as,

$$\vec{U}_p = -\nabla\phi$$

where ϕ is a potential function that satisfies the Laplace equation,

$$\nabla^2 \phi = 0$$

As the solid body surface S is impermeable, the normal component of the velocity must be zero at the wall which gives a Neumann condition of no penetration across the body,

$$\frac{\partial \phi}{\partial n} = \nabla \phi \cdot \vec{n} = \vec{U}_\infty \cdot \vec{n}$$

In practice, the problem is considered in two regions: the solid body and the downstream wake. The body is simulated by a distribution of quadrilateral surface dipoles, μ, and quadrilateral sources, σ. An extra source distribution, σ_{wT}, equal to the transpiration velocity, is introduced to account for viscous effects confined inside the boundary layer. The first row of wake elements is simulated using quadrilateral panel dipoles while further downstream the panels are converted into wake elements formed by straight line vortex filaments, Γ.

$$\nabla \phi = -\frac{1}{4\pi} \int_b (\sigma + \sigma_{wT}) \nabla \left(\frac{1}{r} \right) + \frac{1}{4\pi} \int_b \mu \nabla \left[\frac{\partial}{\partial n} \left(\frac{1}{r} \right) \right] + \frac{1}{4\pi} \int_w \Gamma \nabla \left[\frac{\partial}{\partial n} \left(\frac{1}{r} \right) \right] - \nabla \phi_\infty$$

The unsteady Kutta-Joukowsky condition of zero trailing edge loading is used to release the vortex filaments at body's trailing edge. To satisfy this condition, at each time step a quadrilateral panel with a doublet distribution is created as the first wake panel for each spanwise station. The strength of this panel, Γ_{fst}, is equal to the difference between the corresponding upper and lower trailing edge quadrilateral doublets,

$$\Gamma_{fst} = \mu_u - \mu_l$$

Following Katz and Plotkin [13] the first wake panel is convected downstream from the trailing edge with a 30% of the local undisturbed velocity. Downstream of the first row of wake panels the quadrilateral doublets are transformed into vortex filaments and clustered into vortex elements.

The hybrid free wake model is introduced as an effort to reduce the computational cost of the free wake calculations. The near wake behind the wind turbine is modelled using a free vortex sheet formed by vortex filaments clustered in vortex elements, while the far wake is simulated using a tip or a tip-root vortex model. After a number of wake revolutions of the vortex sheet configuration, the vorticity contained in the vortex sheet is clustered into a tip and root vortex, in a similar way as in Figure 12. In this fashion, the rotor plane induction is maintained at the same time as the number of fluid markers needed to update the wake is considerably reduced.

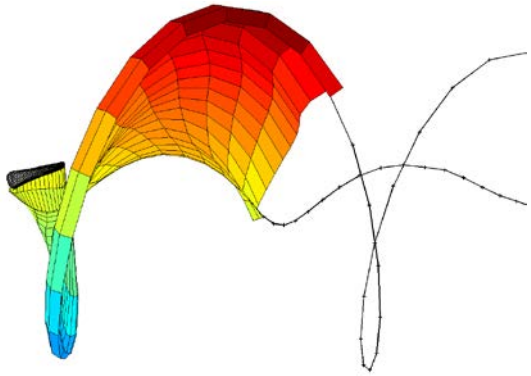

Figure 12: Hybrid free wake model

The motion of the filaments is represented by Lagrangian fluid markers placed at their end points which are convected downstream with the total velocity $\vec{u}$,

$$\vec{u} = \vec{u}_{\infty} + \vec{u}_{body} + \vec{u}_{vsheet} + \vec{u}_{vrtip}$$

where u_{∞} is the freestream velocity, u_{body} is the influence of the solid body, u_{vsheet} is the induction created by the near wake elements and u_{vrtip} is the velocity induced by the far wake root-tip vortex elements.

The velocity induced by the wake vortex filaments is computed by applying the Biot-Savart law. In order to de-singularize its behaviour as r tends to zero, a viscous core is applied to all released vortex filaments during the time updating procedure [14]. In this way an approximation to viscous diffusion, vortex core growth and vortex straining can be included. The Biot-Savart formula is modified as follows,

$$\vec{u}_{wake} = K \frac{\Gamma}{4\pi} \frac{dl \times r}{|r|^3}$$

where K is the kernel parameter, which uses the Scully profile for the vortex filament viscous core [15]. To include the core growth rate, the Squire model is applied by introducing the turbulent eddy viscosity parameter [16]. Bhagwat et al. [17] straining model is used to take into account variations in vortex filament radius due to filament stretching or squeezing.

The inviscid perturbation velocities are calculated on the body surface using a nodal interpolation of the doublets strength, μ. Finally, the unsteady Bernoulli equation is used to compute the surface pressure on each element of the rotor blade,

$$\frac{\partial \phi}{\partial t} + \frac{1}{2}|v|^2 + \frac{p}{\rho} = \frac{p_{ref}}{\rho} + \frac{1}{2}|v_{ref}|^2$$

where v is the total velocity vector, p_{ref} is the far-field reference pressure and v_{ref} is the reference velocity defined as follows,

$$v_{ref} = -\left[V_o + \Omega \times r\right]$$

The viscous boundary layer is solved in a strip manner by using the in-house Q^3UIC code [18]. The Quasi-3D Unsteady Interactive Code, Q^3UIC, is an aerodynamic tool developed for solving the quasi three-dimensional integral boundary layer equations by means of a strong viscous-inviscid coupling with a two-dimensional panel method. In the inviscid part, the airfoil geometry is represented by a surface distribution of constant sources and a parabolic vorticity distribution. The viscous part is taken into account by solving the integral form of the boundary layer r- and θ- momentum equations with extensions for three-dimensional rotational effects, induced by Coriolis and centrifugal forces.

The coupling between the viscous and inviscid parts in the MIRAS code is achieved through the local angle of attack and the transpiration velocity as the coupling parameters. Q^3UIC resolves the boundary layer, calculating the chordwise distribution of the transpiration velocity at each spanwise station along the blade

$$w_T = \frac{1}{\rho} \frac{\partial}{\partial t} \left(\rho u_e \delta_1^* \right)$$

where δ_1^* is the streamwise displacement thickness and u_e is the boundary layer edge velocity. Q^3UIC computations are performed for a given local airfoil geometry and the following non-dimensional parameters:

Reynolds number, ratio between rotational speed and relative velocity, local ratio between chord length and radial position and local angle of attack.

The computed transpiration velocity is introduced into the inviscid three-dimensional panel method as an extra quadrilateral surface source distribution, σ_{wT}, which will move outwards the limiting streamlines around the blades, taking into account the viscous effects into the final solution to the flow problem.

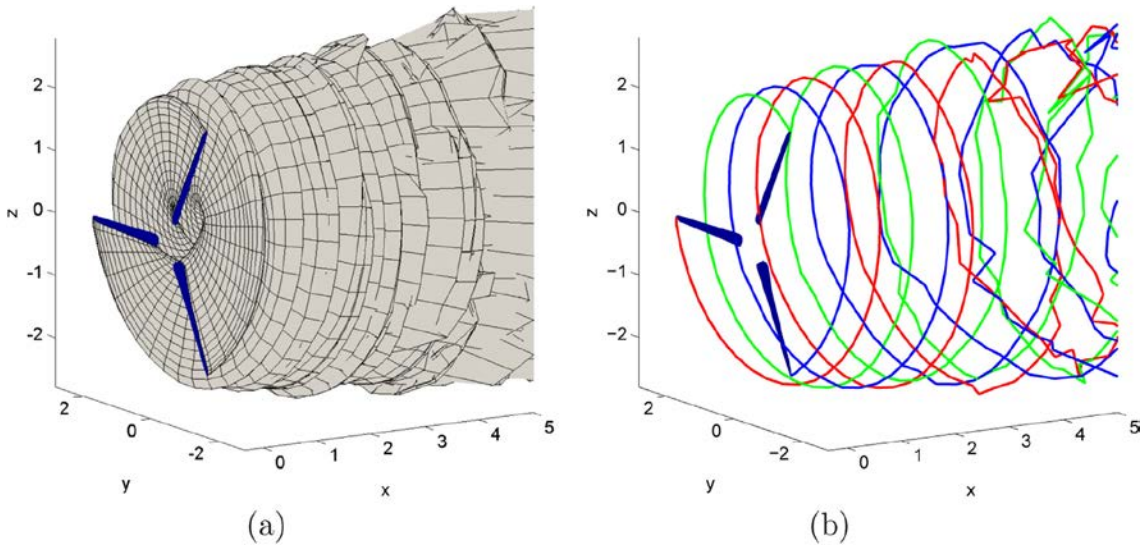

Figure 13: Mexico rotor at TSR = 6.67, (a) full free wake (b) tip vortex filaments

To illustrate the performance of the MIRAS code, validations of the viscous and the inviscid versions of the code are carried out for flows past the MEXICO rotor (Figure 13). In what follows the blade normal and tangential forces are compared against measurements and wake velocities are validated against PIV experimental data. The MEXICO experiment was executed on a three-bladed wind turbine model with a diameter of 4.5m under controlled conditions in the Large Scale Low Speed Facility of the German-Dutch Wind tunnel DNW in a 9.5 x 9.5 m2 open test section. The test cases considered here are the rotor rotating with a constant angular speed of 424.5 rpm at wind speeds of 10, 15 and 24 m/s. The blades are subjected in the three cases to a negative collective pitch of -2.3^o. Instantaneous velocities were extracted in a plane at 9 o'clock when looking downstream at the rotor when the first blade pointed upwards. For more detailed information about the MEXICO experimental campaign, the reader is referred to Schepers and Snel [19].

A surface mesh consisting of 20 spanwise cells and 50 chordwise cells was used for the simulations. A 10^o angular discretization was used for the wake generation and a total amount of 16 wake revolutions was simulated. In this case laminar to turbulent transition was forced at 5% chords from the leading edge on both the upper and lower sides of the airfoil sections.

In Figure 14, the predictions of the normal and tangential blade forces are compared against experimental values for wind speeds of 10, 15 and 24 m/s. As the wind speed increases, the inviscid computations predict higher values for both normal and tangential forces, while the viscous simulations are in much better agreement with the experiment, except in the root region where rotational effects arising from Coriolis and centrifugal forces seem to be under-predicted. At 24 m/s differences between the viscous and the inviscid predictions are enormous; this is related to the existence of regions with trailing edge separation. In Figures 15 and 16 viscous and inviscid velocities are compared against PIV measurements in axial and radial traverses at a wind speed of 24 m/s. The viscous simulations capture much better the axial velocities while the radial and tangential values are more difficult to predict. Overall a good agreement was obtained between the experimental data and the viscous computations.

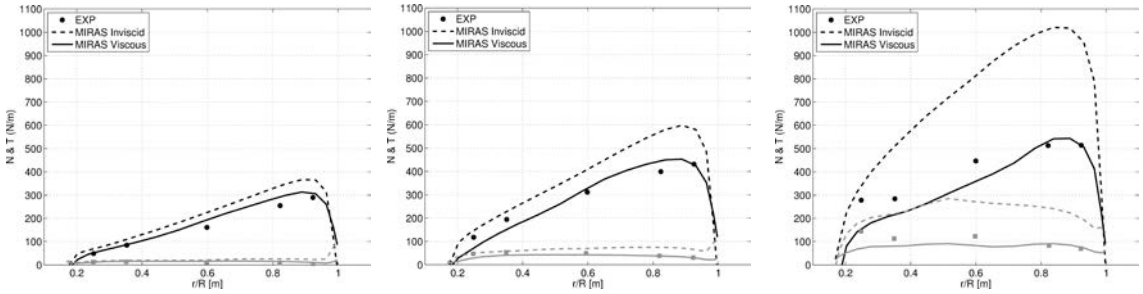

Figure 14: Blade normal and tangential forces at wind speeds of 10, 15, 24 m/s

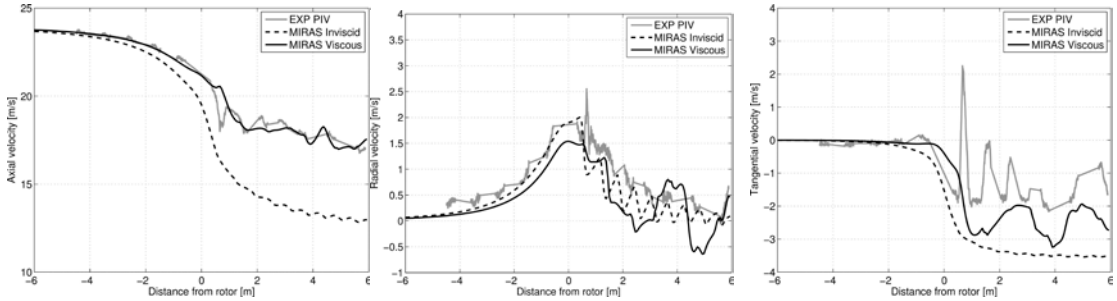

Figure 15: Axial, radial tangential velocity in an axial transverse of r=1.38 m at a wind speed of 24 m/s

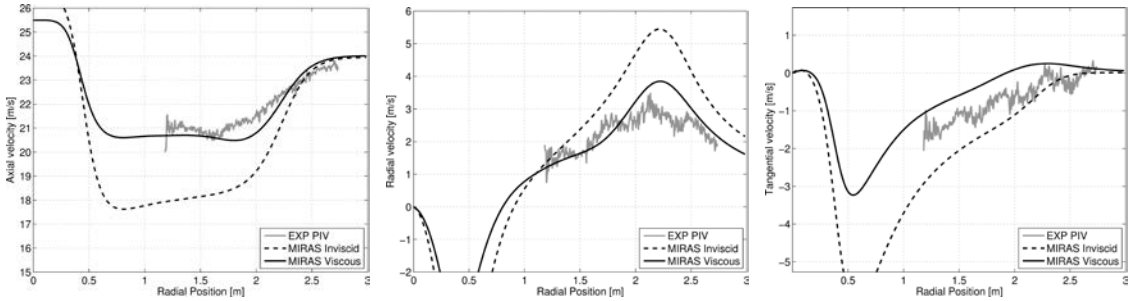

Figure 16: Axial, radial and tangential velocity in a radial transverse of z=0.3 m after the rotor at a wind speed of 24 m/s

1.5.5 Integrated airfoil and blade design

The integrated design of airfoil family and blade can be started from the BEM analysis of an airfoil section at a given blade station. The core of the analysis is the iterative computation of the power coefficient of an airfoil. Because the power performance is an important measure of a blade, it has often been used as a key reference number during design process.

According to the momentum theory, the solution of the power coefficient is maximized when the axial induction factor is a=1/3. With this condition being valid, it can be shown that the power coefficient of an airfoil section can be written as:

$$C_p = \left[(1-a)^2 + x(1+a')^2 \right] x C_t \sigma$$

where the solidity is

$$\sigma = 2F\sin^2(\phi)/C_n$$

a, and a' are the axial and tangential induced velocity interference factors, respectively, x is the local speed ratio, C_t and C_n are the tangential and axial force coefficients, respectively, σ is the rotor solidity, ϕ is the local flow geometry and F is Prandtl's tip loss function.

In the equation above, not all of the variables have been explicitly given except for the axial induction factor that must equal to 1/3. As an idealized design case, the wind shear, turbulence, yaw/tilt and rotational effects are neglected. The other parameters can be divided into two groups. Parameters in group 1 contain the values that will not enter into the BEM iterations. Such as the local speed ratio x, the length of blade R, the number of blades B and the airfoil normal and tangential force coefficients. In each iteration of airfoil optimization, the lift and drag coefficients from the airfoil aerodynamic computations are needed to compute C_t and C_n.

The other group of the variables will be iteratively solved due to their dependency. These parameters are the power coefficient Cp, the local flow angle ϕ and the tangential induction factor a'. The values of Cp, ϕ and a' are initialized with zero before the first BEM iteration. After several iterations, the highest Cp for a blade section at the given flow condition is obtained.

The geometric parameters in group 1 shall be fixed for a given blade design. In the present study, we take the 5MW reference wind turbine [20] as the reference rotor. This reference wind turbine has a maximum rotational speed of 12.1 RPM and a blade length of 63 m. In this task we are going to design a wind turbine rotor with a rated power above 20MW. Therefore the length of the new blade can be approximately estimated

$$R = 63\text{m}\sqrt{(20\text{MW}/5\text{MW})} = 128\text{ m}$$

According to the reference rotor, in the present work we fix the blade length at R=130 m and the tip-speed-ratio (TSR) of 8.

The design variables, design objective and constraints are described in [21] [1] and were summarized in Section 1.5.1.

Since the new airfoils are optimized using previously designed DTU-LN2xx airfoil family, the resulting airfoil will be referred to as DTU-R130-xx airfoils. The designed airfoil family has five airfoils of thickness to chord ratio ranging from 18% to 30%. The optimized airfoil geometries are plotted in Figure 17. To ensure less three dimensional effects due to curvature change along the blade span, the airfoils are designed to have smooth geometrical transition between each other. The shape compatibility is well controlled by the design constraints as shown in the plots.

Some key design values are given in Table 3. The outer part (110-130m) of the blade is constructed with R130-18. The middle part (40-110m) contains R130-21, R130-24, R130-27 and R130-30. Airfoil geometries between these 5 airfoils are obtained by using linear interpolation from the two neighbouring airfoils. The inner part (0-40m) is interpolated between cylinder and R130-30. The corresponding local speed ratios are calculated in the table which are input to the optimization model. For sake of manufacturing, the resulting airfoils have increased trailing edge bluntness along the blade. Considering the blade shape compatibility, the maximum thickness location referred to as xmax/c also increases while thickness increases, seen in the table as well. The design lift and maximum lift for the clean and rough cases are calculated for all the airfoils. According to the design constraints, the difference in Cl between clean and rough cases has to be small. As an example of the R130-18 airfoil, the design lift coefficients Cl_{de} are 1.24 and 1.21 for clean and rough conditions, respectively. In general, all the designed airfoils have good characteristics about roughness sensitivity. The Cp values at different angles of attack are shown in Figure 18. It is found by XFOIL simulation that the Cp values are relatively high for all the airfoils. More importantly the Cp curves are quite flat, i.e. between 5 to 9 degrees. These are the aerodynamic properties expected from the design objective.

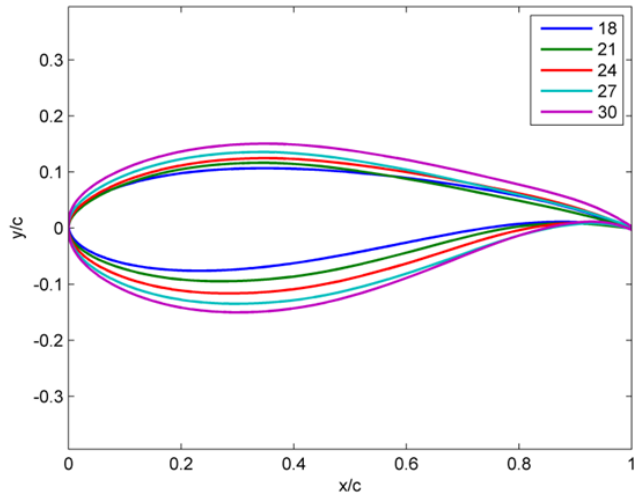

Figure 17: Airfoil shape of the DTU-R130 family

Table 3: Airfoil characteristics and blade parameters

Thickness	18	18	18	21	24	27	30	50	100
Step1: Pre-define blade length and TSR									
r (m)	130	125	110	80	65	50	40	30	0
λ	8	7.69	6.77	4.92	4	3.08	2.46	1.54	-
Step2: Airfoil design based on the local TSR									
Blunt (%)	-	-	0.2	0.23	0.3	0.5	0.6	-	-
x_{max}/c	-	0.278	0.278	0.308	0.314	0.314	0.327	-	100
C_{Lde}	-	-	1.24/1.21	1.25/1.21	1.4/1.34	1.39/1.29	1.41/1.24	-	-
C_{Lmax}	-	-	2.04/2.03	1.97/1.96	1.97/1.95	1.89/1.86	1.89/1.85	-	-
$(C_L/C_D)_{max}$	-	-	146/137	160/130	150/ 119	151/108	132/84	-	-
Step3: Blade construction using the optimal airfoils									
Chord(m)	0	2.4	3.57	4.91	5.37	6.99	8.67	10	7
$\beta(^o)$	-	0.62	0.68	1.65	2.34	4.96	7.7	11	-
ϕ (^{o})	-	5.62	5.68	7.65	9.34	11.96	14.7	18	-
Solidity	-	0.009	0.015	0.029	0.039	0.0668	0.10	-	-
Re ($x10^6$)	-	12.4	16.3	16.4	14.8	15.1	15.4	10	5

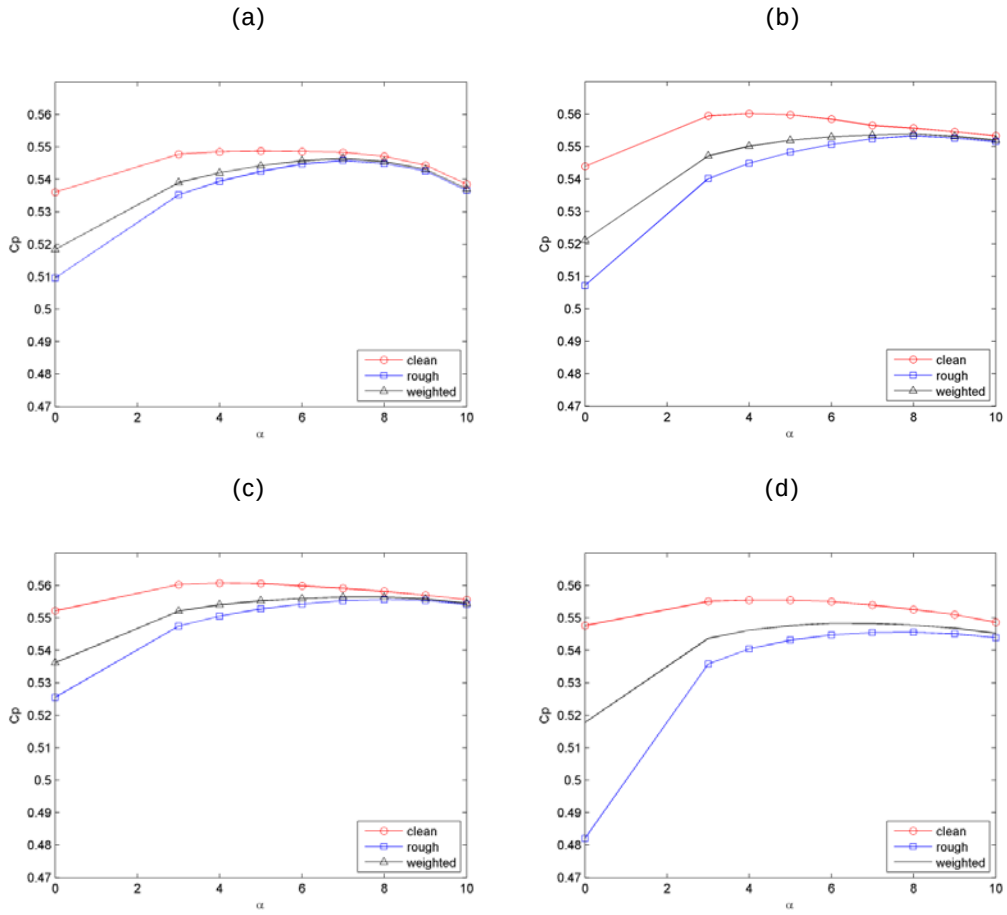

Figure 18: Cp at different AOAs. (a) R130-18; (b) R130-21; (c) R130-24; (d) R130-27; (e) R130-30

1.5.6 Experimental validation of rotor concepts

The experimental rotors are designed using standard Blade Element Momentum (BEM) and blade element (BE) /lifting line (LL) theories. The theories are summarized here.

Blade designed by the 'Standard' BEM Theory

The model BEM developed by Glauert in 1935 is the most commonly used model today for analysis and design of rotors. Nevertheless about the second element of the model, using the momentum theorem, Glauert noted that the angular velocity imparted to the slipstream is very small compared with the angular velocity of the rotor, and that it therefore is possible to simplify the general equations by neglecting certain terms involving the angular velocity and neglecting an influence of lateral pressure forces along the individual stream surfaces. For more details, the reader is referred to [22] [23].

Blade designed by the BE-LL vortex theory

For a more realistic rotor with a finite number of blades, Betz [24] showed that the ideal efficiency is obtained when the distribution of circulation along the blade produces a rigidly moving helicoid wake that moves downstream (in the case of a propeller) or upstream (in the case of a wind turbine) in the direction of its axis with a radial-independent constant velocity wU_∞ where the w is a reduction factor of the wake motion. If the expansion of the wake is neglected, from symmetry, it is readily seen that the induced velocity in

the rotor plane tends to be half of the induced velocity at a corresponding point on the vortex sheet in the far wake or the Trefftz plane: $u_{\theta_0} = \frac{1}{2} u_\theta$ and $u_{z_0} = \frac{1}{2} u_z$. Thus, using the velocity triangle, the induction $W_i = \left(u_{z_0}, u_{\theta_0}\right)$ or relative $V_{rel} = \left(U_\infty - u_{z_0}, \Omega r + u_{\theta_0}\right)$ velocities are found to be

$$u_{z_0} = \tfrac{1}{2} w U_\infty \cos^2 \Phi \text{ and } u_{\theta_0} = \tfrac{1}{2} w U_\infty \cos\Phi \sin\Phi$$

or

$$V_{rel} = U_\infty \left[\left(1 - \tfrac{1}{2} w \cos^2 \Phi\right)^2 + \left(\frac{\lambda r}{R} + \tfrac{1}{2} w \cos\Phi \sin\Phi \right)^2 \right]^{1/2} \text{ and } V_{rel} = \frac{\Omega r + u_{\theta_0}}{\cos\Phi},$$

where $\lambda = \Omega R / V_\infty$ is the tip speed ratio. Using the equation above in axial blade element, we get

$$\frac{dT}{dr} = \frac{1}{2} \rho c N_b C_L U_\infty \left[\left(1 - \tfrac{1}{2} w \cos^2 \Phi\right)^2 + \left(\frac{\lambda r}{R} + \tfrac{1}{2} w \cos\Phi \sin\Phi \right)^2 \right]^{1/2} \cdot \left(\Omega r + u_{\theta_0}\right).$$

Using the LL-vortex theory, the bound vorticity serves to produce a local lift on the blades while the trailing vortices induce the velocity field in the rotor plane. The fundamental expression of the thrust force acting on a blade is most conveniently expressed by the Kutta–Joukowsky theorem, which in the axial projection reads:

$$\frac{dT}{dr} = \rho N_b \Gamma \left(\Omega r + u_{\theta_0}\right).$$

where a dimensionless distribution of circulation or Goldstein's factor *G* was introduced as follows $N_b \Gamma = G h w U_\infty$, *h* is a pitch of the helical vortex structure of the wake behind the rotor which is connected to the tip speed ratio λ and the wake reduction factor *w* by the following relationship

$$h = \frac{2\pi}{\lambda}\left(1 - \tfrac{1}{2} w\right).$$

The final LL vortex theory gives

$$\frac{dT}{dr} = \frac{2\pi\rho}{\lambda} G U_\infty w \left(1 - \tfrac{1}{2} w\right)\left(\Omega r + u_{\theta_0}\right).$$

Equating the right hand sides of blade element and lifting line expressions, a formula to determine the distribution of the chord of the profile SD7003 along the blade for the rotor obtains by BE/LL method:

$$c = \frac{4\pi w \left(1 - \tfrac{1}{2} w\right) G}{\lambda N_b C_L \left[\left(1 - \tfrac{1}{2} w \cos^2 \Phi\right)^2 + \left(\frac{\lambda r}{R} + \tfrac{1}{2} w \cos\Phi \sin\Phi \right)^2 \right]^{1/2}}.$$

where there remains only to determine flow angle ϕ and the Goldstein's factor *G* in each section of the blade. The flow angle ϕ can be expressed according to the velocity triangle by the formula

$$\mathrm{tg}\Phi = \frac{U_\infty - u_{z_0}}{\Omega r + u_{\theta_0}} \equiv \frac{U_\infty}{\Omega r}\left(1 - \tfrac{1}{2} w\right).$$

To define both Goldstein's *G* and reduction *w* factors of the optimal rotor, here we also introduce *an associated vortex system* to the wake which consists of a regular helicoidal sheet extended to infinity in both directions. Although Betz stated the problem of the wake, he was not able to solve the corresponding circulation distribution defining the rotor loading and rotor geometry. Later contributions to solve the problem are due

to the prominent researchers Goldstein and Theodorsen which have considered two partial cases under an incorrect definition of the helical pitch *h*. In the following, the different solution steps of this problem will be presented. Introducing the dimensionless wind power coefficient, we get

$$C_P = 2w\left(1-\tfrac{1}{2}w\right)\left(I_1-\tfrac{1}{2}wI_3\right),$$

where $I_1 = 2\int_0^1 G\left(x,h\right)xdx$ is the mass coefficient and $I_3 = 2\int_0^1 G\left(x,h\right)\dfrac{x^3dx}{r^2+\left(h/2\pi\right)^2}$ is the axial energy factor.

The coefficients I_1 and I_3 depend on both Goldstein's *G* factor and the wake pitch *h*. To determine the Goldstein's *G* factor for different operating conditions with a fixed pitch *h*, a usual procedure from lifting line theory is followed. The lifting line of continuous circulation along blades is replaced with *N* discrete segments of a constant bound circulation and at each ends $N+1$ trailing vortices is attached that has the half magnitude of induction velocity as the *associated vortex system*. In a cylindrical coordinates - $\left(z,r,\theta\right)$ for the related helical filament with a linear circulation γ and placed at radius r_0, the induced velocity in point *r* is given as follows

$$u_r = \frac{-\gamma}{2\pi r}\frac{\sqrt[4]{\left(l^2+r^2\right)\left(l^2+r_0^2\right)}}{l}\operatorname{Im}\left[\frac{e^{i\chi}}{e^{\mp\xi}-e^{i\chi}}\pm\frac{l}{24}\left(\frac{2l^2+9r_0^2}{\left(l^2+r_0^2\right)^{3/2}}-\frac{2l^2+9r^2}{\left(l^2+r^2\right)^{3/2}}\right)\ln\left(1-e^{\pm\xi+i\chi}\right)\right]$$

$$u_z = \frac{\gamma}{2\pi l}\begin{Bmatrix}1\\0\end{Bmatrix}+\frac{\gamma}{2\pi l}\frac{\sqrt[4]{l^2+r_0^2}}{\sqrt[4]{l^2+r^2}}\operatorname{Re}\left[\frac{\pm e^{i\chi}}{e^{\mp\xi}-e^{i\chi}}+\frac{l}{24}\left(\frac{3r^2-2l^2}{\left(l^2+r^2\right)^{3/2}}+\frac{9r_0^2+2l^2}{\left(l^2+r_0^2\right)^{3/2}}\right)\ln\left(1-e^{\xi+i\chi}\right)\right]$$

$$u_\theta = \left(u_0-u_z\right)l/r,$$

where $\chi=\theta-z/l$; $u_0=\gamma/2\pi l$; $h=2\pi l$; $e^{\xi}=\dfrac{r'}{r_0'}=\dfrac{r}{r_0}\dfrac{\left(l+\sqrt{l^2+r_0^2}\right)\exp\left(\sqrt{1+\left(r/l\right)^2}\right)}{\left(l+\sqrt{l^2+r^2}\right)\exp\left(\sqrt{1+\left(r_0/l\right)^2}\right)}$.

In the notation of "$\pm$" or "$\mp$", the upper sign corresponds to $r<r_0$, and the lower one to $r>r_0$. Furthermore, a collocation point is placed in the middle of each segment. There are now $N+1$ unknown circulations of the discrete helical filaments and correspondingly, there are *N* equations. The problem can be closed by the resulting equation with a zero of the total vortex strengths being determined under the Betz rotor condition. To achieve a high accuracy, 100 discrete helical vortex filaments are applied. To validate the model, the results were compared to the computations by an original simulation of the Goldstein's solution.

For each given helicoidal wake structure, the power coefficient is seen to be uniquely determined, except for the parameter *w*. Differentiating of C_p, with respect to *w* yields the maximum value of C_p, resulting in

$$w(C_P=C_{P,\max})=\frac{2}{3I_3}\left(I_1+I_3-\sqrt{I_1^2-I_1I_3+I_3^2}\right).$$

There is a need for detailed experimental testing of both designing methods described here. The experiment took place in the water flume of length 35 m, width 3 m and operative height of 0.9 m at DTU.

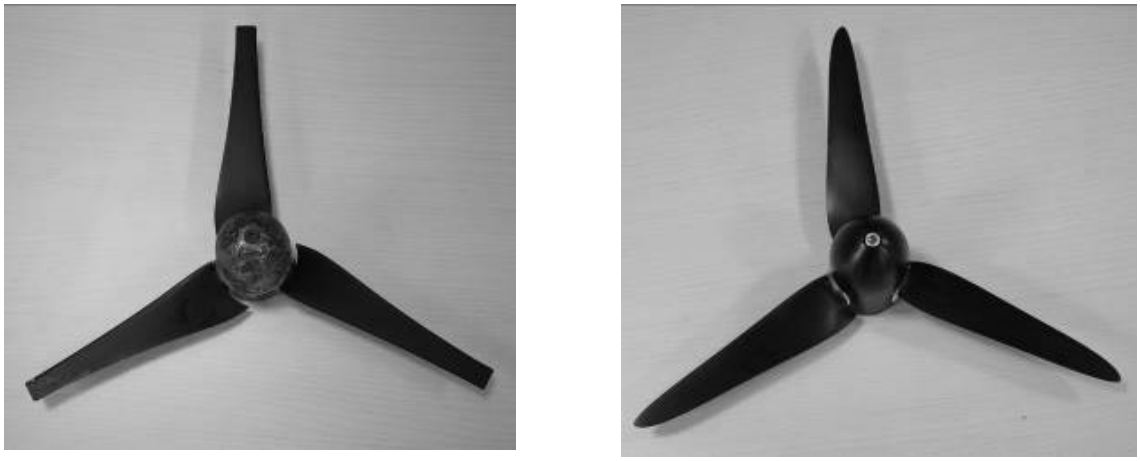

Figure 19: Photos of both rotors designed with the BE/M (left) and BE/LL (right) theories

At present, two laboratory models of both three-bladed rotors have been created for such comprehensive experimental study (Figures 19 and 20). Both models have the same diameter D = 0.376m with blades of length 0.159 m consisting of SD7003 airfoil sections.

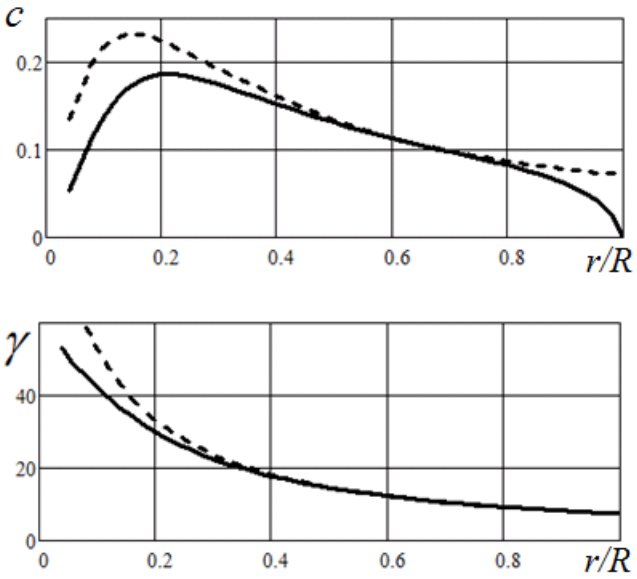

Figure 20: Distribution of the chord *c* and pitch angle γ along the blade span designed with the BE/M (dashed line) and BE/LL (solid line) methods

The free flow speed in the flume was U_∞ = 0.64m/s. In order to filter out disturbances, the water was led through an inlet equipped with honeycomb. The velocity profile of the incoming water flow is about constant with a variation of less than 1% during all experiments, measured with LDA and an independent OTT Z400 velocimetry. The Reynolds numbers based on rotor diameter and free stream velocity was varied in the range 140 000 <Re< 240 000. As the working fluid, tap water at a temperature of 20ºC was used.

The rotor was driven by a JVL Industri Elektronik MAC400 servo motor which was operated at a constant rotational speed within 2% accuracy. The torque of the motor was transferred to the rotor axis via a rigid gear transmission. Measurements of the rotor characteristics were conducted by strain sensors installed in the rotor mounting. The power (C_P) and thrust (C_T) coefficients were measured for different tip speed ratios,

λ = 3-9, and blade pitch angles coinciding to different values of the angle of attack, α = 1°-12°. The angle of attack of the blade was fixed for each test case.

As a result of the direct experimental comparison in Table 4 it was established for the first time that the rotor designed with the BE-LL method allows earning more kinetic energy from an incoming uniform flow. The C_P achieves maximum values (indicated as bold figures in the table) for both rotors under equal values of two tip speed ratios, λ = 5 or 6, and an ordinal angle of attack, α = 5.5°. These data indicate slight different values from that initially put in both models where λ was exactly equal to 5 and α is not far to 4.5°.

Table 4: Comparison C_P of both rotors designed by BE/LL (upper dark lines) and BE/M (lower white lines) methods

α \ λ	**3**	**4**	**5**	**6**	**7**	**8**	**9**
1°	0.02	0.04	0.22	0.27	0.19	0.07	-0.07
	0.01	0.02	0.14	0.28	0.21	0.09	-0.06
4°	0.09	0.23	0.42	0.42	0.39	0.33	0.27
	0.07	0.15	0.37	0.38	0.35	0.26	0.04
5.5°	0.11	0.30	**0.43**	**0.43**	0.40	0.35	0.28
	0.10	0.25	**0.40**	**0.40**	0.36	0.29	0.20
7°	0.13	0.35	0.42	0.42	0.39	0.33	0.22
	0.12	0.34	0.38	0.37	0.31	0.21	0.05
8.5°	0.17	0.37	0.40	0.38	0.31	0.18	0.04
	0.14	0.35	0.35	0.31	0.20	0.01	-0.20
9°	0.18	0.35	0.35	0.29	0.15	0.02	-0.19
	0.14	0.29	0.27	0.18	-0.00	-0.24	-0.53
12°	0.22	0.28	0.20	0.04	-0.18	-0.49	-0.91
	0.19	0.21	0.05	-0.16	-0.47	-0.91	-0.79

1.5.7 Design of low noise wind turbine rotors

The main goal of the rotor design is to investigate how much the noise emission of medium and large wind turbines could be reduced by using the new airfoil family and redesigning the blade planform. In the scope of the project, the comparisons are carried out between an existing turbine of 3 MW (NM80) and a new turbine of matching power; and the design of a 10 MW low noise turbine rotor. The steps in designing the blades are the following:

1. The airfoils on the reference turbine are replaced with the airfoils from the series DTU-(LN)2xx.
2. The relative thickness distribution on the blades is adjusted to match the new airfoils. This results with a thicker blade in case of the medium power turbine, and a more slender large turbine blade.
3. Initial twist distribution is changed to match the design angle of attack of the series DTU-(LN)2xx. The pitch angle is calculated from the optimal flow angle applying the BEM theory.
4. Using an optimization algorithm, the chord and twist layouts are modified to yield the highest possible power while reducing emitted noise.

The optimization algorithm

The numerical optimization is performed in MATLAB 2015a using the Optimization Toolbox. The appropriate solver for such a smooth non-linear problem is “fmincon”. The function “fmincon” attempts to find a minimum of a nonlinear multivariable function subjected to linear and non-linear constraints starting at an initial estimate [25]. The objective function in this project is to maximize the annual energy production (AEP) and therefore directly maximize the power output. The set constraints are geometrical requirements (the chord

and twist were to monotonically decrease towards the tip), maximum thrust and the emitted noise restricted by the recommended noise limit in regulations.

The project follows Danish regulations which state that sound pressure level A-weighted (SPL [dB(A)]) of the turbines may not exceed in open countryside 44 dB(A) at a wind speed of 8 m/s (at 10 m height) and 42 dB(A) at 6m/s; and in areas with noise-sensitive land use 39 dB(A) at 8 m/s and 37 dB(A) at a wind speed of 6 m/s. Due to concerns about large wind turbines, the added constraint for the 10MW turbine is maximum low frequency SPL (<160Hz) should not exceed 20 dB(A) indoor at both wind speeds, irrelevant of the land use [26].

Aero-acoustic noise of turbines can be identified at 5 distinct sources - turbulent inflow noise, turbulent boundary layer trailing edge noise, airfoil trailing edge bluntness noise, laminar vortex shedding noise and tip noise. Due to the turbulent nature of the flow on the turbine blade, the laminar vortex shedding noise is irrelevant for this analysis.

The noise from turbine is predicted using a modified Brooks-Pope-Marcolini model (BPM) [27] to calculate the airfoil self-noise and Amiet's turbulence inflow model [28] to calculate inflow noise. Brooks et al. derived semi-empirical scaling laws from a series of noise measurements on a NACA0012 airfoil. In the model, boundary layer displacement thickness is a crucial parameter in calculating airfoil self-noise. Given the airfoils used in the scope of the project are not as thin as NACA0012 nor symmetrical, the boundary layer parameters are calculated with XFOIL.

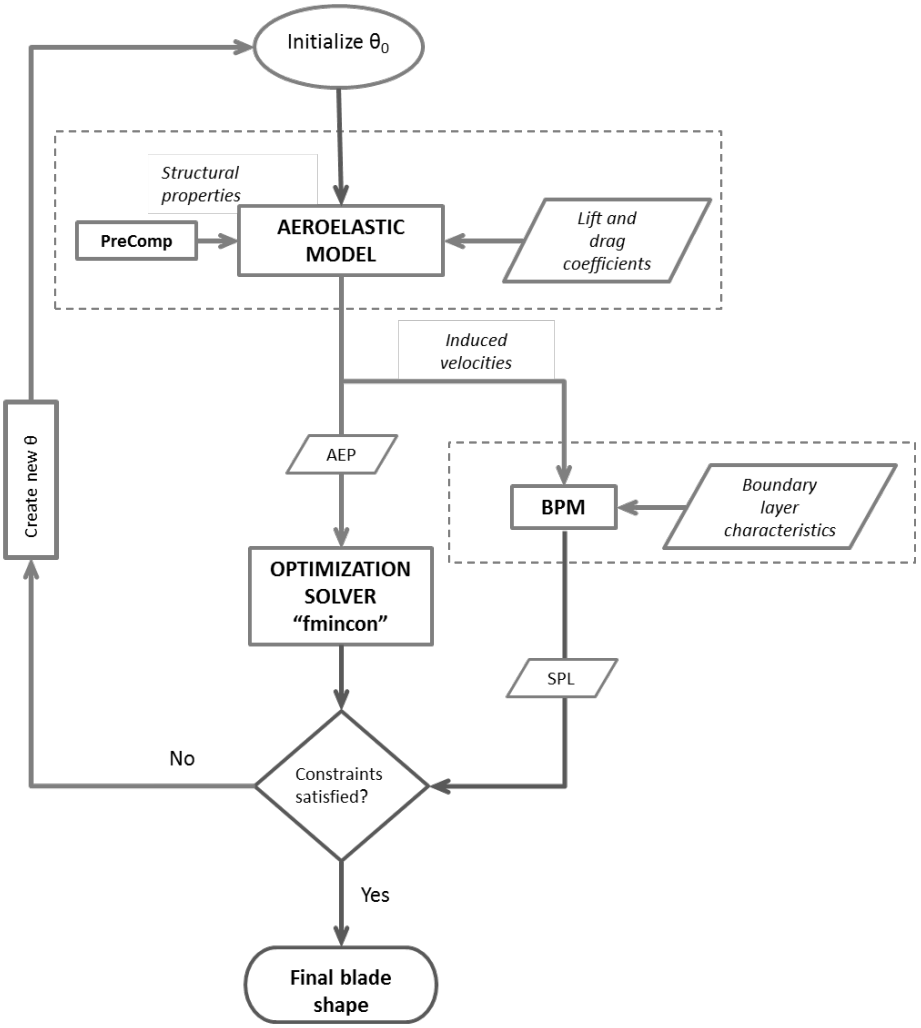

Figure 21: Schematic display of the optimization algorithm for the low noise blade design

The turbine performance is computed with an in-house aeroelastic code. The code is a simple dynamic model of the turbine with 13 degrees of freedom [29]. The tabulated aerodynamic airfoil properties are obtained with XFOIL. The structural properties of the new blade are calculated using PreComp, a pre-processor for computing composite blade properties developed by NREL [30]. The noise model is connected to the aeroelastic code through the induced velocities on the blade. The overall optimization algorithm is shown in Figure 21.

The new medium size low noise turbine

Figure 22 shows the thickness distribution of the new blade. The reference 3 MW turbine provided from LM is built of airfoils from the series NACA634xx, with xx going from 15% to 24% of relative thickness. When those airfoils are replaced with the series DTU-(LN)2xx, the relative thickness of the outboard part of the new blade is larger since the thinnest airfoil in the new series is 18% relative thickness.

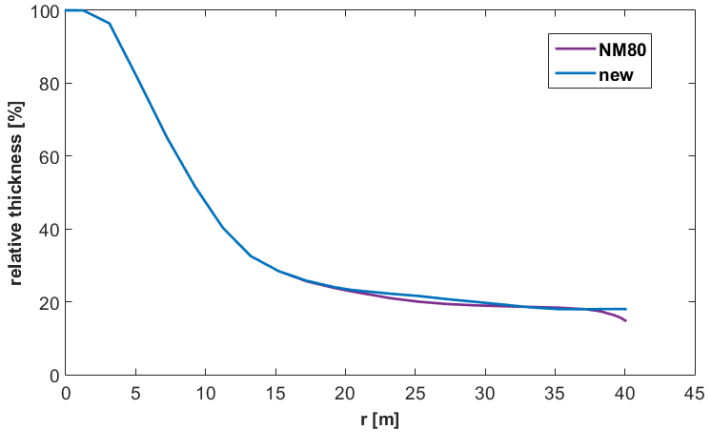

Figure 22: Thickness distribution of the new blade. The tip part of the blade is 18% relative thickness; the reference turbine has the minimum thickness of 15%

Figure 23 and Figure 24 show the new optimized chord and twist distributions. The new turbine has an increased outboard chord but the length of the tip chord is the same. The new pitch angle is significantly reduced in comparison with the reference turbine. Figures 25-28 display the performance of the reference rotor and the newly designed rotor. Since the new airfoil series DTU(LN)2xx are high lift airfoils with supreme performance, the new blade had to be pitched 4.5° to match the power of the reference turbine. The annual energy production of the new rotor is 5.131 GWh while the reference turbine has an AEP of 5.115 GWh. For further noise reductions, the blade is pitched with extra 1.5° degree at low wind speeds; the power reduction is compensated at wind speeds before the rated so the AEP with that set-up is 5.129 GWh which is slightly bigger than the AEP of the reference turbine.

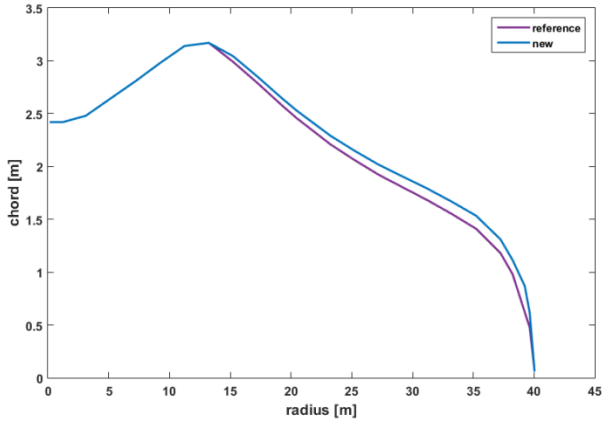

Figure 23: Chord distribution of the new 3MW blade in comparison with the reference turbine

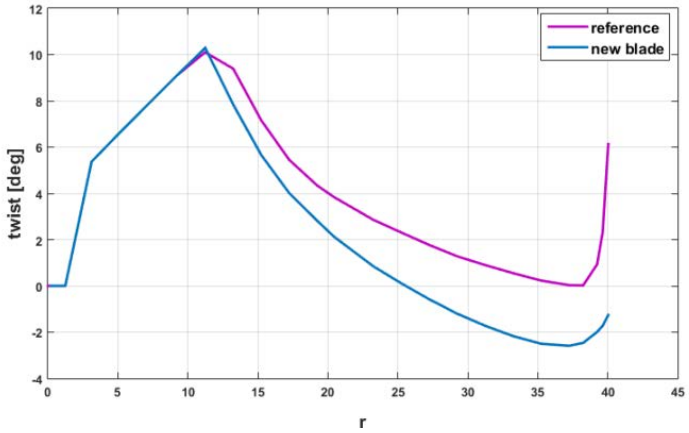

Figure 24: Twist distribution of the new blade in comparison with the reference turbine

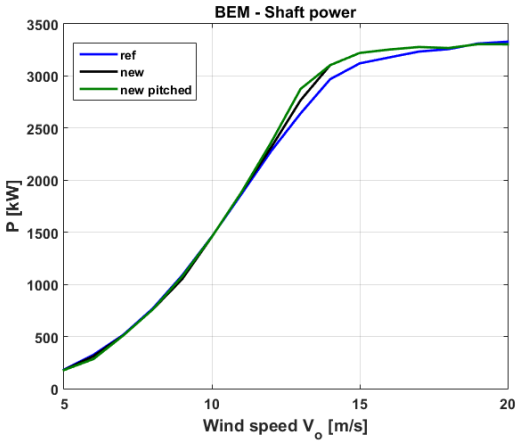

Figure 25: Comparison of the calculated power outputs of the reference turbine and the new 3MW turbine. The new turbine is pitched additionally 4.5° over the whole range of wind speeds to match the power of the reference turbine

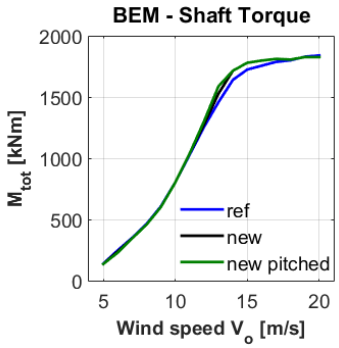

Figure 26: Comparison of the calculated torque of the reference turbine and the new 3MW turbine

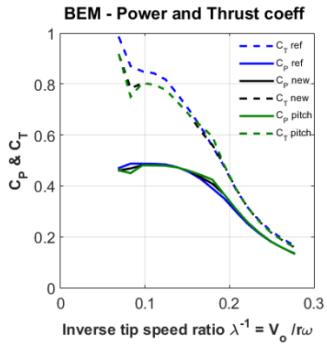

Figure 27: Comparison of the calculated power and thrust coefficients of the reference turbine and the new 3MW turbine

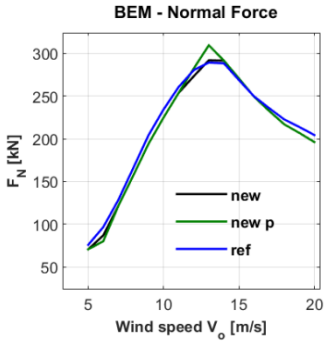

Figure 28: Comparison of the calculated normal forces of the reference turbine and the new 3MW turbine

The overall sound pressure levels (SPL) and sound power levels (PWL) are reduced (see Table 5) especially in the cases with rough surface conditions which are also the conditions during the majority of the turbine life cycle. Figure 29 shows the total sound pressure levels of the new turbine with clean and rough surface. With added roughness, the frequency peak is shifted a bit towards the lower frequencies. This can be seen in the overall SPL levels for low frequencies (10-160Hz). Figures 30 and 31 show the total SPL level of the reference and the new turbine at clean and rough surface conditions. For further noise reduction, the new blade is pitched with extra 1.5° at low wind speeds (Figures 32 and 33) while keeping the AEP sufficiently high.

The hub height wind speed is corrected to the wind speed of 6 m/s at a height of 10 m. Observer height for the analysis is 1.5 m and roughness length z_0 was 0.05 m in accordance to the regulations. The considered atmospheric conditions are to be during night time with turbulence intensity σ = 3% and wind shear α = 0.015.

As can be noted, the new turbine at clean conditions has a frequency shift towards the higher frequencies. This means that the low frequency noise (frequencies of 10 – 160 Hz) of the new turbine is lower in comparison to the reference turbine. When looking at the SPL A-weighted, the total difference is smaller due to the frequency shift. The C-weighting filters out noise also at the higher frequencies so the total SPL(C) reflects better the total noise reduction. The frequency bandwidth in the analysis is one-third octave.

Figure 34 shows the noise from different sources on the new turbine. The turbulent boundary layer noise and the inflow noise are the dominant sources as expected. Figure 35 depicts the comparison of SPL levels of the two turbines versus their power curve (new turbine is pitched 4.5° over the whole range of wind speeds to match the power of the reference turbine).

Table 5: Total sound power levels (PWL) and sound pressure levels (SPL) of the reference and the 3MW new turbine, without and with A- and C weighting. Wind speed 6 m/s corrected to a height of 10 m. Observer height = 1.5m, observer distance is 80 m, turbulence intensity σ = 3%, wind shear α = 0.015 and roughness length z_0 = 0.05 m. The SPL_low is for the frequencies 10-160 Hz.

		PWL	PWL(A)	SPL	SPL(A)	SPL(C)	SPL_low	SPL_A_low
clean	reference	95.35	87.02	44.45	36.12	43.15	42.45	22.12
	new	93.10	86.20	42.19	35.30	39.89	40.86	15.97
	reduction	**2.25**	**0.82**	**2.25**	**0.82**	**3.26**	**1.59**	**6.15**
	new extra 1.5° pitch	92.25	85.18	41.33	34.26	39.02	40.00	15.24
	reduction	**3.1**	**1.84**	**3.12**	**1.86**	**4.13**	**2.45**	**6.88**
rough	reference	94.90	87.33	43.99	36.42	42.60	41.73	20.33
	new	93.82	85.89	42.91	34.98	41.01	41.36	18.49
	reduction	**1.07**	**1.44**	**1.07**	**1.44**	**1.59**	**0.38**	**1.83**

new	93.00	84.73	42.08	33.82	40.17	40.06	18.1
extra 1.5° pitch							
reduction	**1.9**	**2.6**	**1.91**	**2.6**	**2.43**	**1.67**	**2.23**

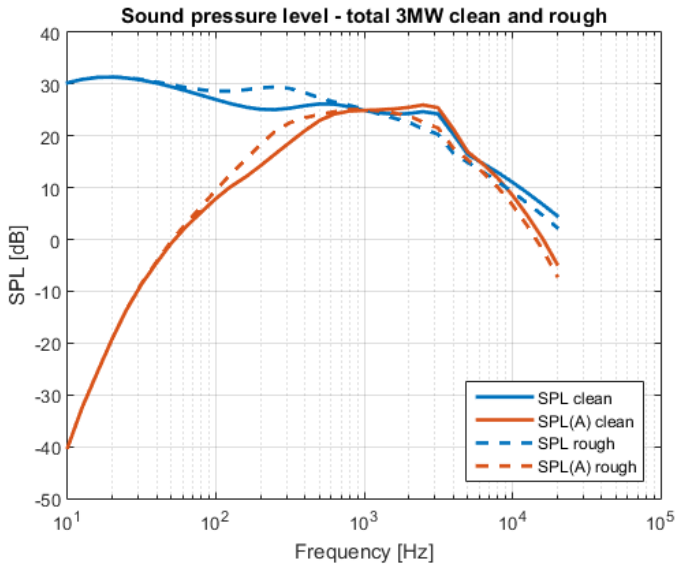

Figure 29: Comparison of sound pressure levels of the new 3MW turbine with clean and rough surface conditions. Wind speed at 6 m/s corrected to a height of 10 m. Observer height = 1.5 m, observer distance is 80 m, turbulence intensity σ = 3%, wind shear α = 0.015 and roughness length z_0 = 0.05 m

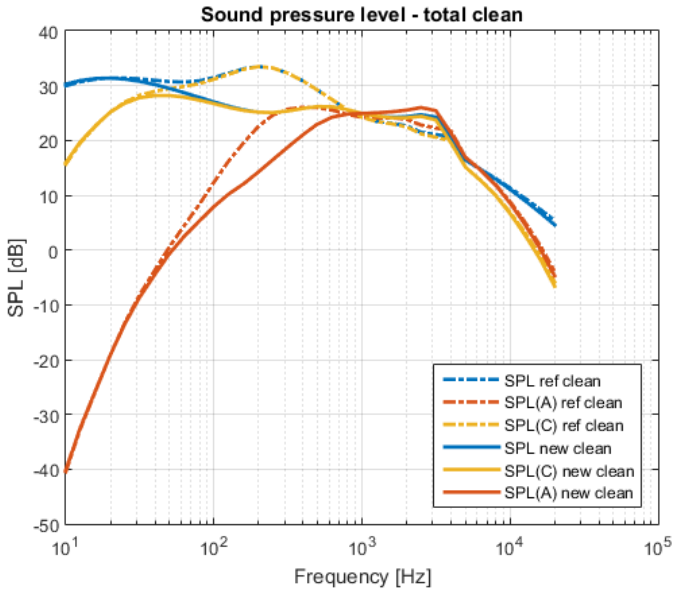

Figure 30: Comparison of sound pressure levels of the reference turbine and the new 3MW turbine at 6 m/s corrected to a height of 10 m. Observer height = 1.5 m, observer distance is 80 m, turbulence intensity σ = 3%, wind shear α = 0.015 and roughness length z_0 = 0.05 m, clean surface conditions

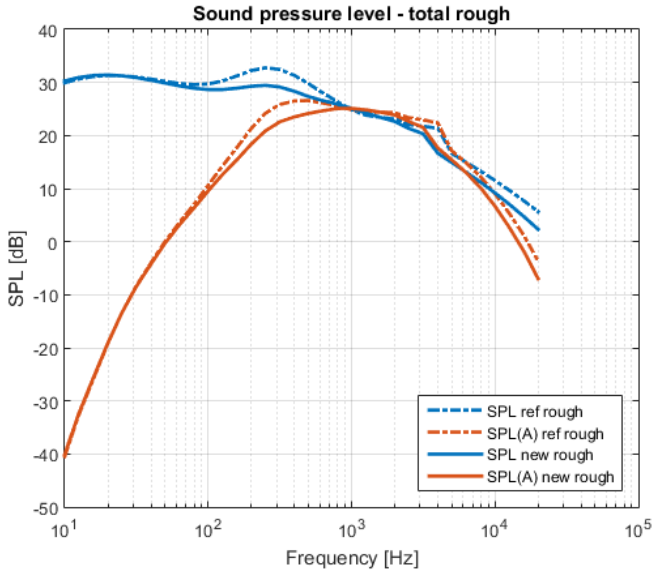

Figure 31: Comparison of sound pressure levels of the reference turbine and the new 3MW turbine at 6 m/s corrected to a height of 10 m. Observer height = 1.5 m, observer distance is 80 m , turbulence intensity σ = 3%, wind shear α = 0.015 and roughness length z_0 = 0.05 m, rough surface conditions

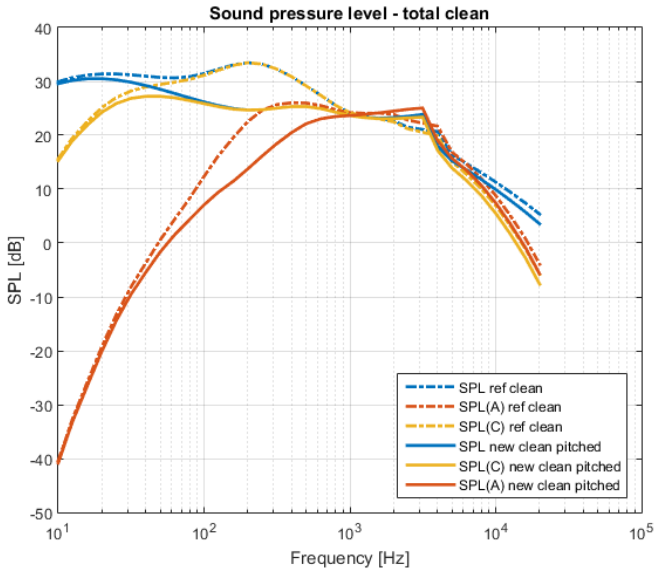

Figure 32: Comparison of sound pressure levels of the reference turbine and the new 3MW turbine with extra 1.5° pitch at 6 m/s corrected to a height of 10 m. Observer height = 1.5 m, observer distance is 80 m, turbulence intensity σ = 3%, wind shear α = 0.015 and roughness length z_0 = 0.05 m, clean surface conditions

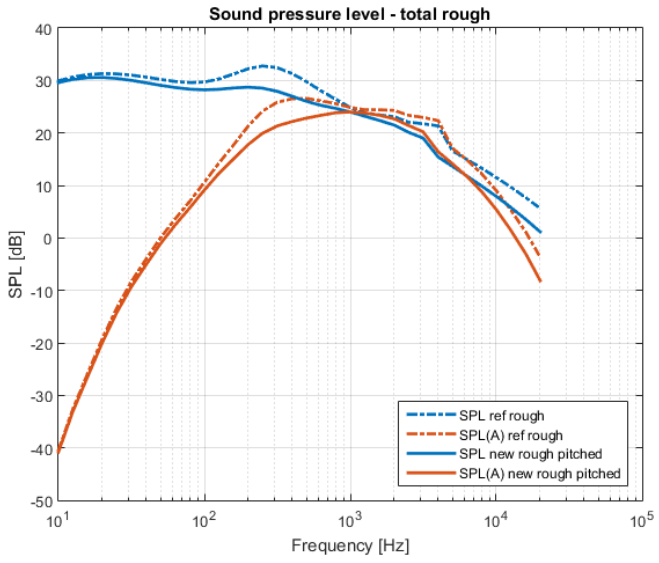

Figure 33: Comparison of sound pressure levels of the reference turbine and the new 3MW turbine with extra 1.5° pitch at 6 m/s corrected to a height of 10 m. Observer height = 1.5 m, observer distance is 80 m, turbulence intensity σ = 3%, wind shear α = 0.015 and roughness length z_0 = 0.05 m, rough surface conditions

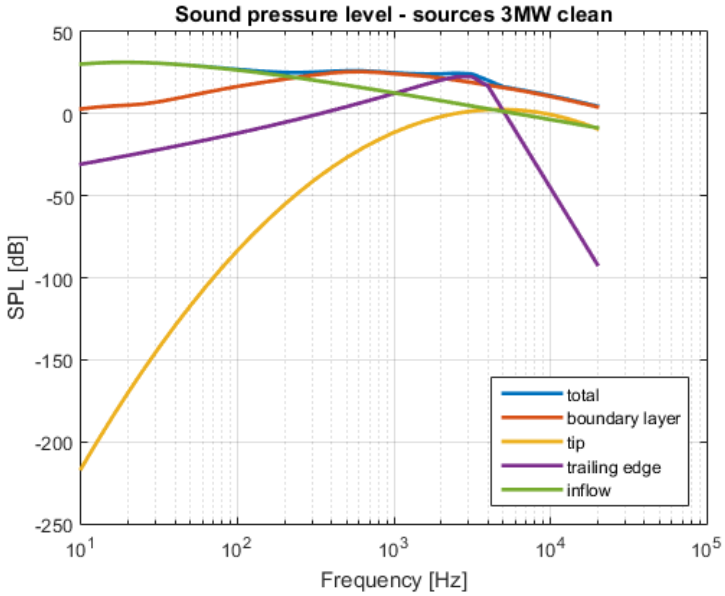

Figure 34: Calculated noise from different sources on the new 3MW turbine at 6 m/s corrected to a height of 10 m. Observer height = 1.5 m, turbulence intensity σ = 3%, wind shear α = 0.015 and roughness length z_0 = 0.05 m, clean surface conditions

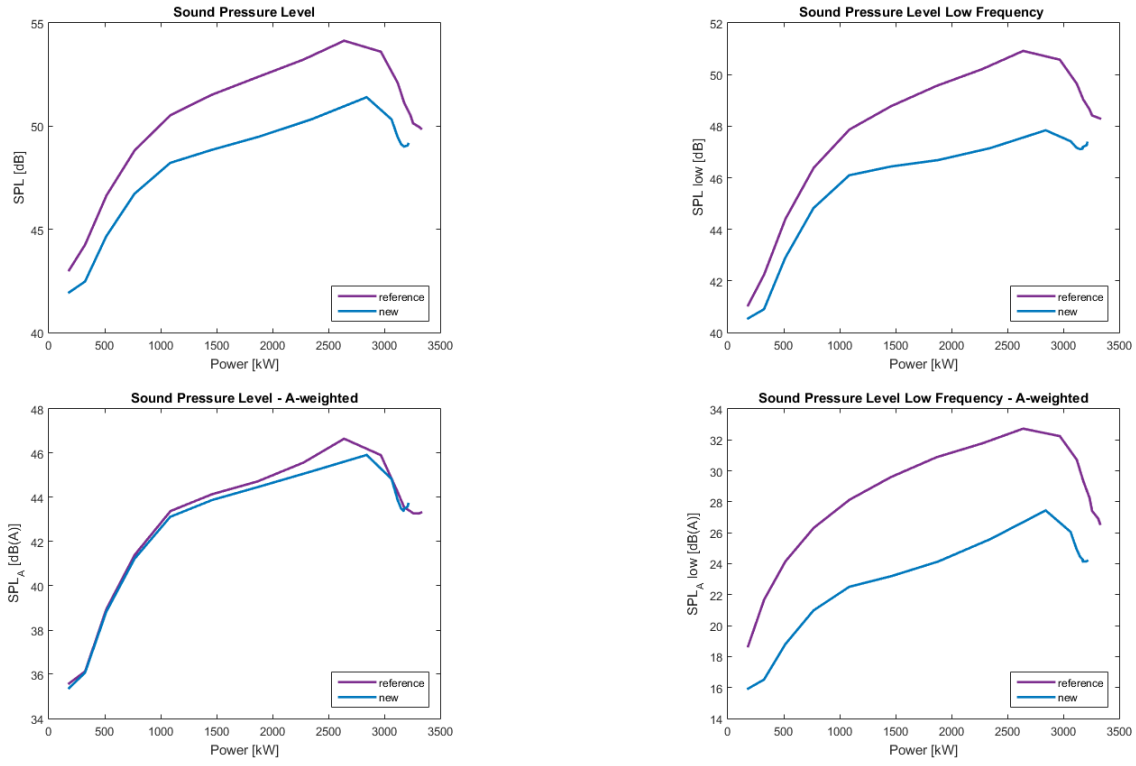

Figure 35: Comparison of Sound Pressure Levels of the reference turbine and the new 3MW turbine at different power levels. Observer height = 1.5 m, observer distance 80 m, turbulence intensity σ = 3%, wind shear α = 0.015 and roughness length z_0 = 0.05 m

The new large low noise wind turbine

Figure 36 shows the thickness distribution of the new blade. The reference turbine is built of airfoils from the series FFA-W3-xxx, with relative thickness from 24% to 48%. The decision is made to make a new slender blade with the series DTU-(LN)2xx, so the relative thickness of the outboard part of the new blade is smaller and the tip airfoil is 18%. Another critical design parameter is the maximum tip speed and it is limited to 80 m/s. The reference turbine which was designed for offshore applications has a rated rotational speed of 1.005 rad/s which gives around 90 m/s tip speed. The maximum rotational speed of the new blade is reduced to 0.897 rad/s.

Figure 37 shows the twist distribution of the new blade. The twist angle is adjusted to the airfoil design angle of 5°. The new twist angle is increased in comparison with the reference turbine. The new optimized chord distribution is shown in Figure 38. The chord is reduced in the mid-section of the blade but is slightly increased towards the tip. This blade planform results in significant noise reduction while keeping the performance high.

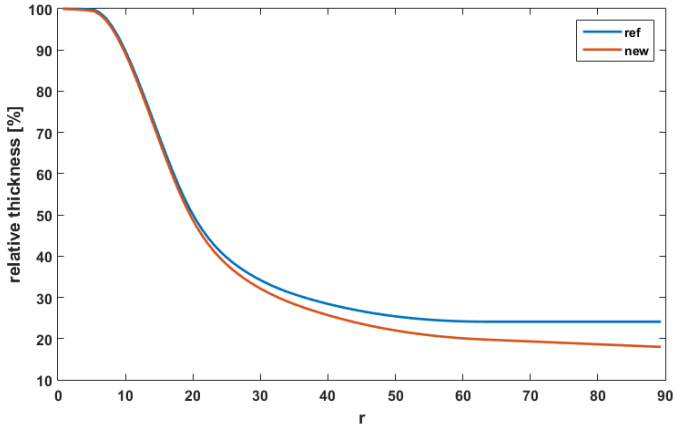

Figure 36: Thickness distribution of the new 10MW blade. The tip part of the blade is 18% relative thickness; the reference turbine has the minimum thickness of 24%

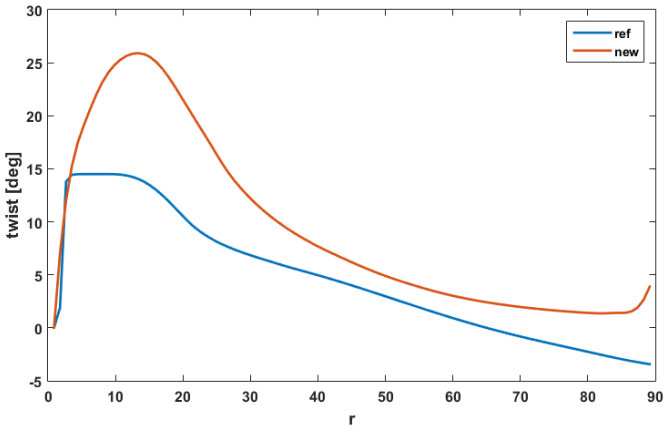

Figure 37: Twist distribution of the new 10MW blade in comparison with the reference turbine

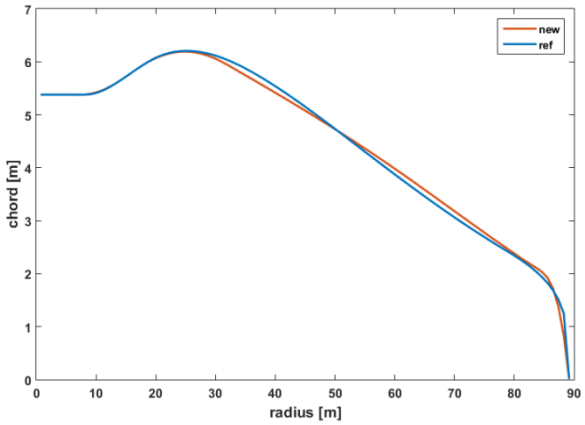

Figure 38: Optimized chord distribution of the new 10MW blade with respect to the reference blade.

Figure 39-42 display the performance of the reference turbine and the newly designed turbine. The new turbine exhibits slightly lower power at low winds speeds but the overall annual energy production is higher – the AEP of the new turbine is 23.67 GWh, and the reference turbine is 22.49 GWh. The rated mechanical power (without gearbox losses) of the new turbine calculated with BEM theory is 10.6 MW

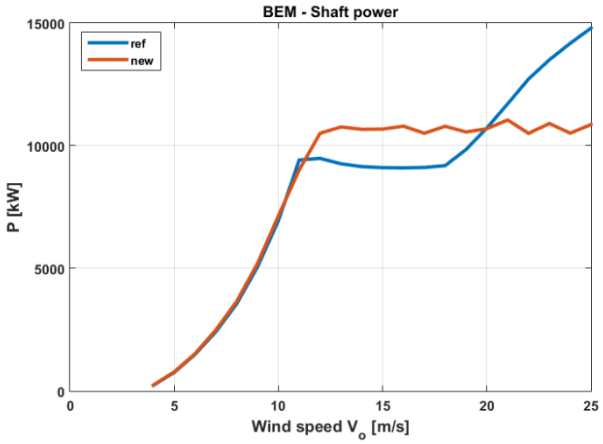

Figure 39: Comparison of the calculated power outputs of the reference turbine and the new 10MW turbine. The new turbine has a reduced rated rotational speed of 0.897 rad/s to limit the tip speed to 80m/s

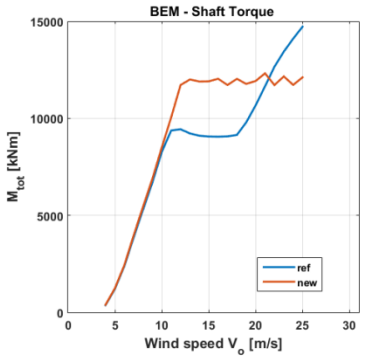

Figure 40: Comparison of the calculated power outputs of the reference turbine and the new 10MW turbine

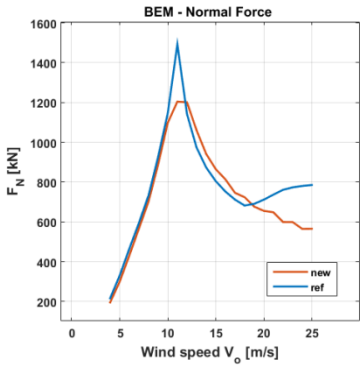

Figure 41: Comparison of the calculated normal forces of the reference turbine and the 10MW new turbine

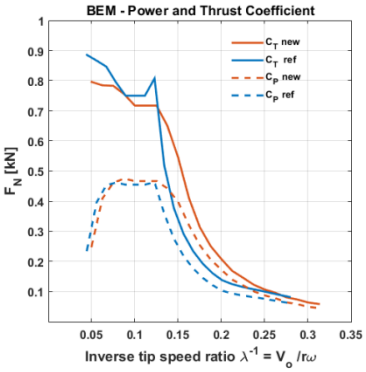

Figure 42: Comparison of the calculated power and thrust coefficients of the reference turbine and the new 10MW turbine

The overall sound pressure levels (SPL) and sound power levels (PWL) are significantly reduced. Figure 43 and Figure 44 show the total SPL level of the reference and the new turbine in clean and rough surface conditions. The hub-height wind speed is corrected to the wind speed of 8 m/s at a height of 10 m. Observer height for the analysis was 1.5 m and roughness length z_0 was 0.05 m in accordance to the regulations. The considered atmospheric conditions were to be during night time with turbulence intensity σ = 3% and wind shear α = 0.015. The frequency bandwidth in the analysis is one-third octave. The total sound power and sound pressure levels are listed in the Table 6. Considering turbines of power 10MW would be placed offshore or in less sensitive areas, the SPL(A) of the new turbine is within the Danish regulations (max 44 dB(A) at 8 m/s). With the rough surface conditions, there is a frequency shift towards lower frequencies in comparison to the reference turbine what can also be seen in the total SPL values for the low frequencies (10-160 Hz). However, the SPL(A) calculated indoors is still well below the level required by the Regulations (20 dB(A)). The differences between SPL of the new rotor under clean and rough conditions are plotted in Figure 45. Figure 46 shows the noise from different sources on the new turbine. The turbulent boundary layer noise and the inflow noise are the dominant sources as was expected.

Table 6: Total sound power levels (PWL) and sound pressure levels (SPL) of the reference and the 10MW new turbine, without and with A-weighting. Wind speed 8 m/s corrected to a height of 10 m. Observer height = 1.5m, observer distance is 209 m , turbulence intensity σ = 3%, wind shear α = 0.015 and roughness length z_0 = 0.05 m. SPL(A) indoor is calculated according to [26] with ground correction for offshore turbine. The SPL_low is for the frequencies 10-160 Hz.

		PWL	PWL(A)	SPL	SPL(A)	SPL_low	SPL_A_low	SPL(A) indoor
clean	reference	110.79	105.06	52.21	46.47	48.30	28.31	12.20
	new	106.80	98.96	48.21	40.37	46.24	25.26	9.44
	reduction	**3.99**	**6.1**	**4**	**6.1**	**2.06**	**3.05**	**2.76**
rough	reference	110.08	105.20	51.50	46.61	47.59	26.21	10.39
	new	107.67	98.50	49.08	39.91	47.46	27.57	11.63

reduction	**2.41**	**6.7**	**2.42**	**6.7**	**0.13**	**-1.36**	**-1.24**

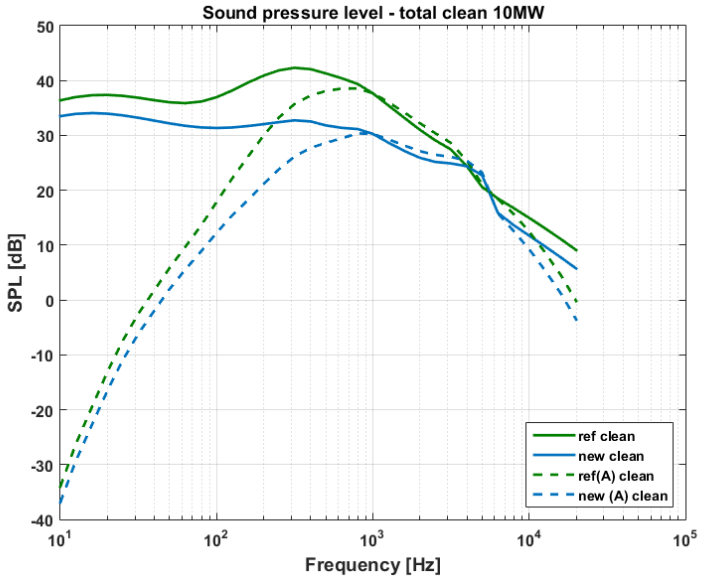

Figure 43: Comparison of sound pressure levels of the reference turbine and the new 10MW turbine at 8 m/s corrected to a height of 10 m. Observer height = 1.5 m, observer distance is 209 m, turbulence intensity σ = 3%, wind shear α = 0.015 and roughness length z_0 = 0.05 m, clean surface conditions

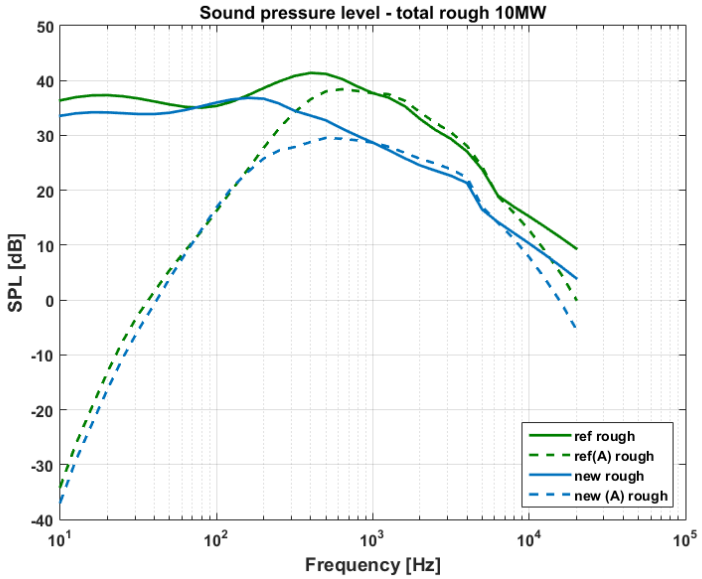

Figure 44: Comparison of sound pressure levels of the reference turbine and the new 10MW turbine at 8 m/s corrected to a height of 10 m. Observer height = 1.5 m, observer distance is 209 m, turbulence intensity σ = 3%, wind shear α = 0.015 and roughness length z_0 = 0.05 m, rough surface conditions

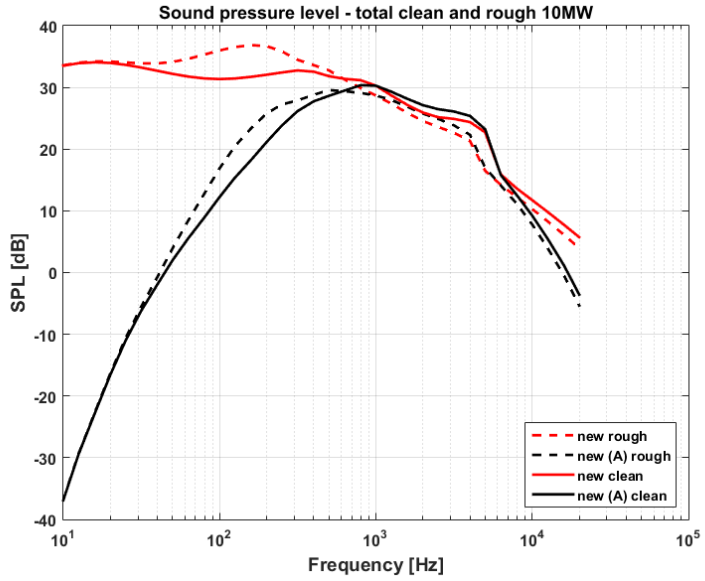

Figure 45: Comparison of sound pressure levels of the new 10MW turbine at clean and rough surface conditions. Wind speed 8 m/s corrected to a height of 10 m. Observer height = 1.5 m, observer distance is 209 m, turbulence intensity σ = 3%, wind shear α = 0.015 and roughness length z_0 = 0.05 m

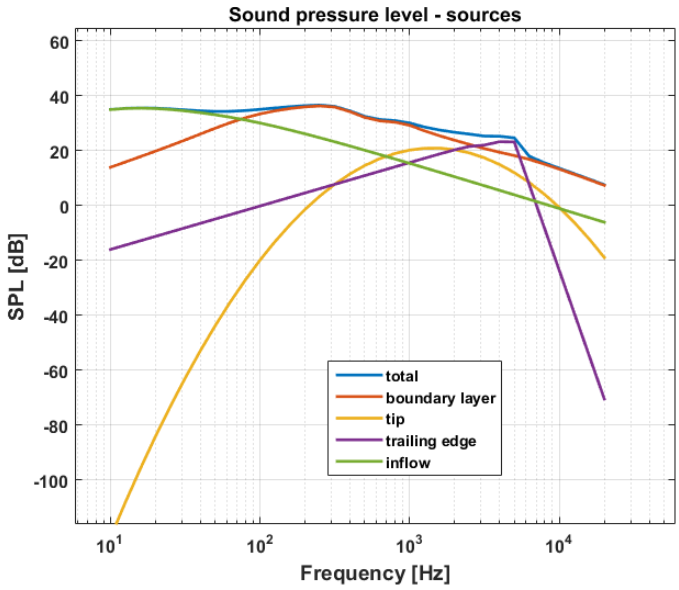

Figure 46: Calculated noise from different sources on the new 10 MW turbine at 8 m/s corrected to a height of 10 m. Observer height = 1.5 m, turbulence intensity σ = 3%, wind shear α = 0.015 and roughness length z_0 = 0.05 m, clean surface conditions

1.5.8 CFD validations

In this work-package, CFD is used to validate both designed airfoils and rotors. Some results have been presented in previous sections with wind tunnel results.

RANS validation of the new thin airfoils

This sub-section presents results from EllipSys2D with Reynolds Averaged Navier-Stokes turbulence (RANS) model. Comparisons between results computed with different numerical tools are performed. The newly designed thin airfoil family is simulated by CFD, Xfoil and Q^{3}UIC programs.

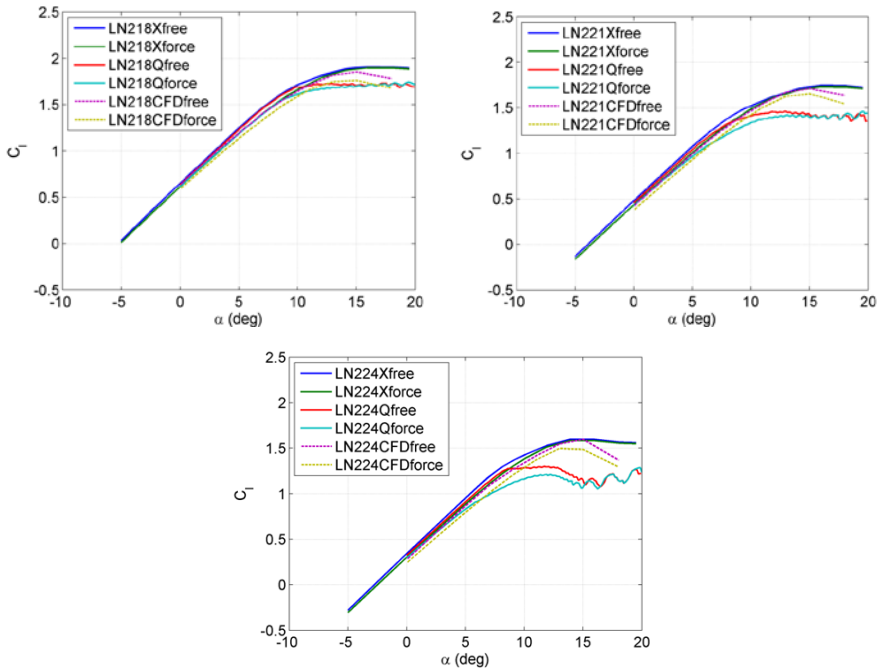

Figure 47: Comparisons of lift coefficient using different numerical methods

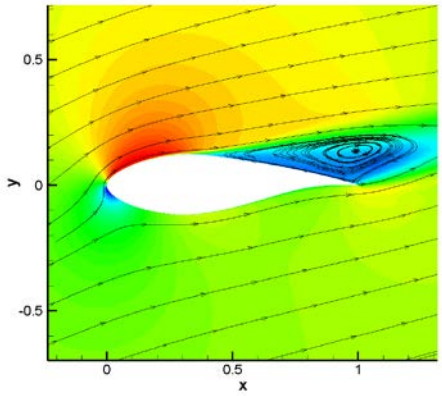

Figure 48: Velocity contour with stream lines of the flow past a DTU-LN224 airfoil at Re=3x10^6 and angle of attack of 18^o

The flows over the DTU-LN218, LN221, LN224 airfoils are simulated at a Reynolds number of 3x10^6 which is aimed at the Reynolds number of modern wind turbines. The angle of attack (AoA) is from 0 to 18 degrees which also covers the possible AoA of wind turbine flow condition. To represent the surface roughness, free transition and full turbulent cases are considered. According to the design criteria, the difference between the

clean and rough cases should be as small as possible. The results of lift coefficient are shown in Figure 47. As an example, the flow past the DTU-LN224 airfoil is shown in Figure 48.

It can be concluded from the simulations that

- CFD results indicate low roughness sensitivity for the new airfoils.
- For C18 airfoil, Xfoil, Q^3UICK and CFD agree well.
- For LN221 and LN224 airfoils, CFD and Xfoil results are closer but usually over-predict after stall. Q^3UIC code had also encountered stability problem after stall especially for thicker airfoils.

LES validation of LN118 airfoil together with noise prediction and reduction

The present numerical study is aimed at validations against the wind tunnel measurements for both aerodynamics and aeroacoustics. Therefore, the airfoil geometry and flow conditions are set according to the experiments:

- Airfoil: CQU-DTU-LN118 airfoil, chord=0.6 m, span=1.8 m (0.6 m used for noise integration), serration length=16.7% chords
- Angles of attack: 0 degree and 8 degrees. (geometrical angle in the wind tunnel)
- Wind speed=45 m/s. Sound speed=344 m/s.
- TE types: (a) original TE (without serration), (b) TE with serration: 16.7%-chord.

It is worth noting that the computations are performed for both original airfoil and the original airfoil with a TE serration.

Figure 49 shows the pressure coefficient on the wall surface, the geometry of the TE serration is also seen from the plot. It is observed that there is no evident variation of pressure in the spanwise direction, which means that aerodynamic performance is hardly influenced by the serration. Figure 50 shows the difference between the measured pressure coefficient and the LES results. At an angle of attack of -1.34^o (0^o wind tunnel geometrical angle), general agreements are observed between the measured data and the computations of two types of airfoils. Figure on the right hand side is the case for an angle of attack 6.07^o which shows same trend but with some better agreements. It is also expected that LES works better at a relative larger angle of attack where the size of turbulence eddies is relatively bigger.

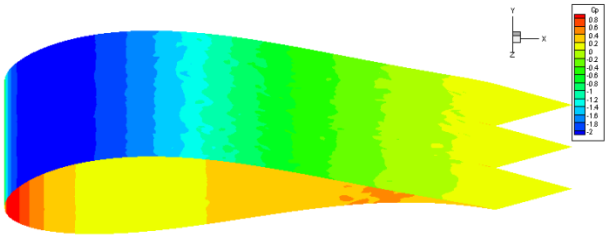

Figure 49: Normalized wall surface pressure

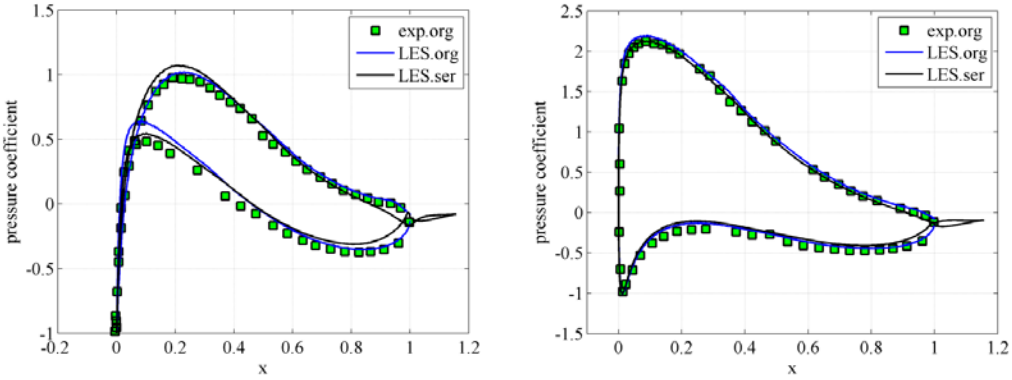

Figure 50: Cp compared at geometrical angles of attack 0° and 8°

At the retarded or emission time, the thickness and loading noise equations are written as

$$4\pi p'_T(\vec{x},t) = \frac{\partial}{\partial t}\int_{f=0}\left[\frac{\rho_0 v_n}{r(1-M_r)}\right]_{res} dS$$

$$4\pi p'_L(\vec{x},t) = \frac{1}{c}\frac{\partial}{\partial t}\int_{f=0}\left[\frac{p\cos\theta}{r(1-M_r)}\right]_{res} dS + \int_{f=0}\left[\frac{p\cos\theta}{r^2(1-M_r)}\right]_{res} dS$$

Even though the aerodynamic field is so similar for the non/serrated airfoils, the generated sound field has larger deviations, see Figure 51. At the small angle of attack, the noise level is reduced in the higher frequency range, as shown in the figure. The experimental data shows no noise reduction at frequencies below 2 kHz. On the numerical side, a larger noise reduction is seen in the high frequency range but a small reduction at low frequencies is also observed. In Figure 51, as the angle of attack is increased, the noise spectra are shifted towards low frequency as compared to the case of 0° angle of attack. As the suction side boundary layer thickness increases with angle of attack, the noise spectrum calculated on the airfoil suction side shifts to the low frequency range. On the contrary to the previous case, the noise reduction is only observed at frequencies below 2 kHz. It seems that at the larger angle of attack, the noise spectra are not affected by the serration at higher frequencies at all. As low frequency noise propagates for a longer distance, it makes sense to implement TE serrations at the outer part of blade where angle of attack is similar as the case shown in Figure 51. There are many other factors that might influence the efficiency of the serration, such as the serration length (root to tip length), wave length (width), flap angle (attached angle at TE), etc. It is expected that TE noise can be reduced for most kind of serration shapes before stall angle of attack.

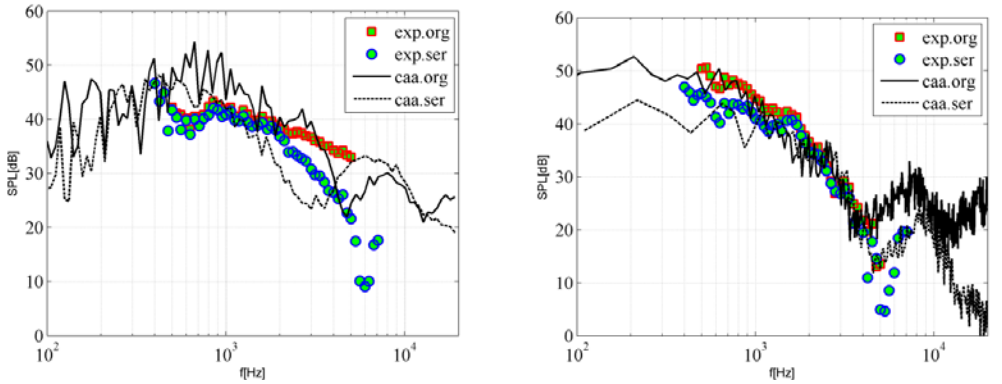

Figure 51: Comparisons of simulated noise spectra against measurements at an angle of attack of 0° (left) and an angle of attack of 8°

Effect of compressibility

As the wind turbine rotor size becomes larger, the compressibility effect might be included in the design procedure. Therefore, based on the original designed in-house airfoils, further designs are carried out to include the effect of compressibility. The design objectives and constraints are kept the same as before and new airfoils are obtained after a number of iterations by including the Mach number effect. The airfoil profiles designed at a Mach number of 0.35 are shown in Figure 52. It is seen that there is some small change of the shape for both airfoils. But in general, the compressibility has no big influence on the airfoil aerodynamics. The lift and drag variations are shown in Figures 53 and 54 for the 18% and 21% airfoils, respectively. The new design has some limited improvements on the lift but also a slightly increased drag.

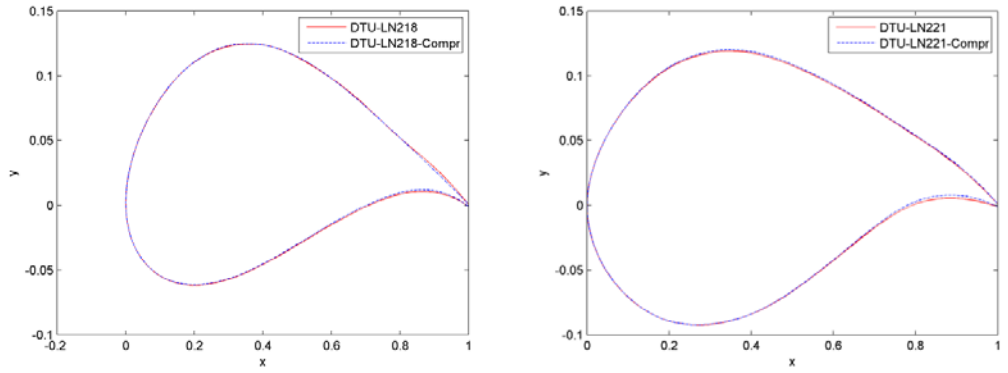

Figure 52: The airfoils designed with and without compressibility effect

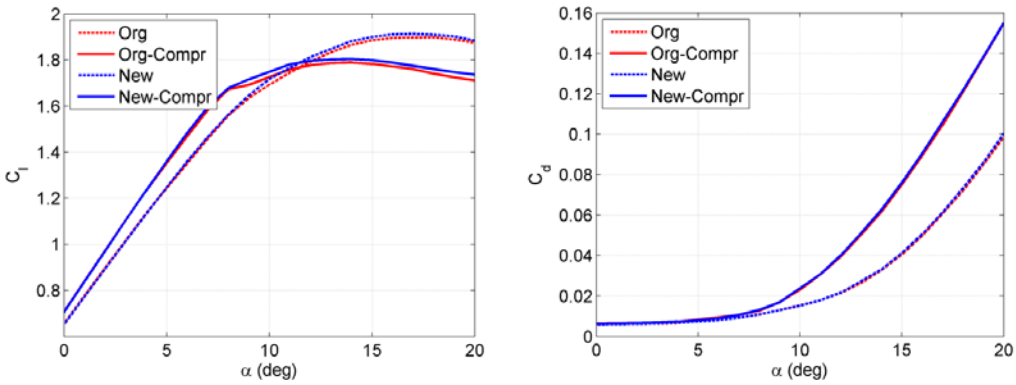

Figure 53: DTU-LN218 and modified LN218: free transition

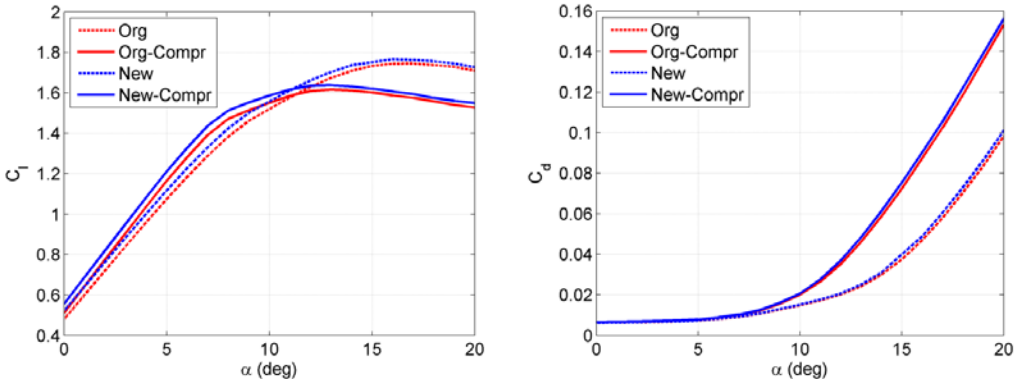

Figure 54: DTU-LN221 and modified LN221: free transition

Modification of the RANS model for thick airfoil calculations

In this part of work, RANS calculations are performed for thick airfoils at large angles of attack. The airfoils under investigation are the DU-96-W350 airfoil and the FFAW310 airfoil, and both airfoils have relative thickness larger than 30%. Over-prediction of forces is often seen in the RANS simulations, typically for thick airfoils and/or at high angles of attack.

By looking at the *k-ω SST* model, it combines the *k-ω* model of Wilcox in the inner region of the boundary layer and the standard *k-ε* model in the outer region and the free steam outside the boundary layer. The transport equations are written as follows:

$$\frac{Dk}{Dt} = \frac{\tau_{ij}}{\rho}\frac{\partial U_i}{\partial x_j} + \frac{\partial}{\partial x_j}\left[\left(\nu + \sigma_k \nu_t\right)\frac{\partial k}{\partial x_j}\right] - \beta^* \omega k$$

$$\frac{D\omega}{Dt} = \frac{\gamma}{\rho \nu_t}\tau_{ij}\frac{\partial U_i}{\partial x_j} + \frac{\partial}{\partial x_j}\left[\left(\nu + \sigma_\omega \nu_t\right)\frac{\partial \omega}{\partial x_j}\right] + 2(1-F)\sigma_{\omega 2}\frac{1}{\omega}\frac{\partial k}{\partial x_j}\frac{\partial \omega}{\partial x_j}$$

For the base line model (BSL), the eddy-viscosity is defined as $\nu_t = \frac{k}{\omega}$.

And for the SST model $\nu_t = \frac{a_1 k}{\max(a_1\omega, \Omega F_2)}$, with a_1=0.3.

Our new model is based on the advantages of Menter's SST model and Coakley's model:

$$\nu_t = \frac{a_1 k}{a_1(1-\beta)\omega + \beta \max(a_1\omega, \Omega F_2)}$$

The formulation is similar to Coakley's model. For β=1, the model is reduced to the SST model (with modified constant a_1=0.275); for β=0, the model is reduced to BSL model. The model is specially designed for turbulent airfoil flows due to the weighting coefficient:

$$\beta = \min(1, 0.5 + t/c).$$

Results of the DU-96-W350 airfoil at a Reynolds number of 3×10^6 is shown in Figure 55. An improvement of the RANS model is seen from the comparison to the experimental data. In the linear lift region, the two models both agree with the data. However, the original RANS model largely over-predicts the lift after stall angle of attack. In the computations of the FFAW310 airfoils, the difference of the two RANS models might be observed from Figures 56 and 57 in terms of flow separation. The original model has not predicted well the flow separation while the modified model triggered separation earlier.

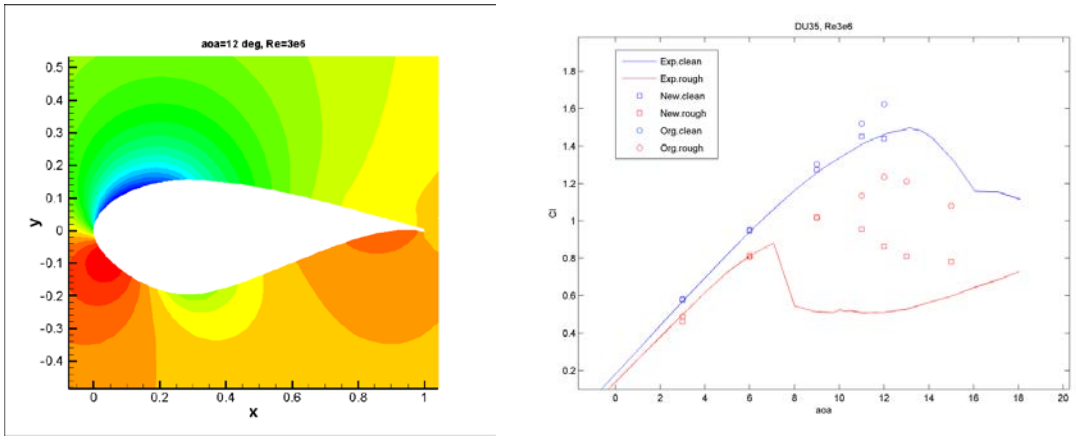

Figure 55: Pressure contours (left) and lift comparisons (right)

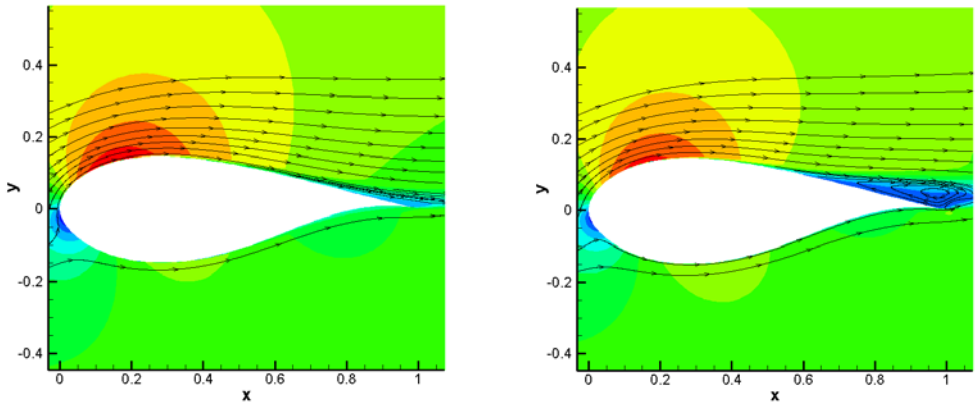

Figure 56: Velocity contours calculated from the original (left) and modified (right) RANS models

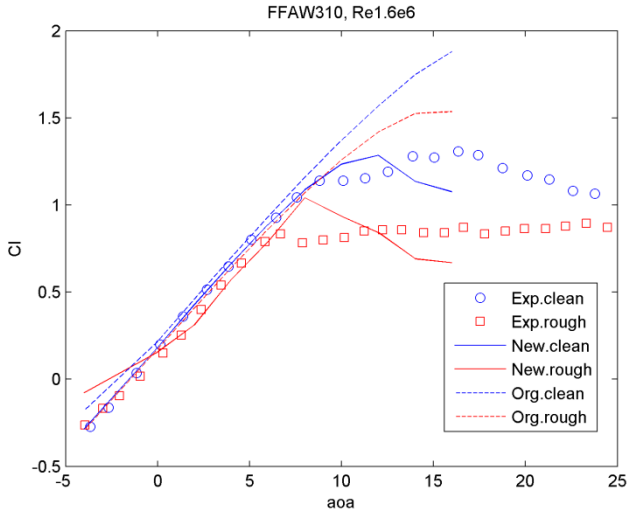

Figure 57: Comparisons of the lift curves

Validations of 2D aerodynamic design tools with 3D rotor simulation

So far within this project, all the airfoils and rotor blades are designed with 2D aerodynamic tools, typically with Xfoil and Q^{3}UIC. The validity of the 2D methods can be either proved by rotor experiments or full rotor CFD calculations. In the current study, two of the newly designed in-house rotors are selected for validations. The rotor sizes of the two wind turbines are 40m and 130m which yields rated power of 3MW and 20MW, respectively. Apart from the size of the two turbines, the validations should have covered a large range of MW size wind turbines. The input of airfoil data to the BEM model is obtained from Xfoil calculations. By comparing the force distributions calculated from BEM (based on 2D airfoil data) and from CFD (based on full 3D flow), it is possible to identify the influence from the 2D design tools. Figure 58 shows results of the 3MW wind turbine, the force distributions from the two methods agree well, for both wind speeds at 10 m/s and 15 m/s. The same observation is found in Figure 59 for the 20MW wind turbine simulations. From this point of view, the 2D aerodynamic tools are reliable. However, it is also noticed that a larger difference is seen at a wind speed of 15m/s (Figure 58 (right)). In this case, flow separation is seen from the CFD calculations in the blade inboard part. The BEM calculation based on 2D airfoil data over-predicted the loading in the flow separation region. In Figure 60, the influence of the thickness is seen by a closer look at the pressure distribution in the outboard (y=80m) and inboard (y=40m) part of the blade. This implies that, more attention should be paid to design the airfoils at blade inboard part, i.e., thick airfoils.

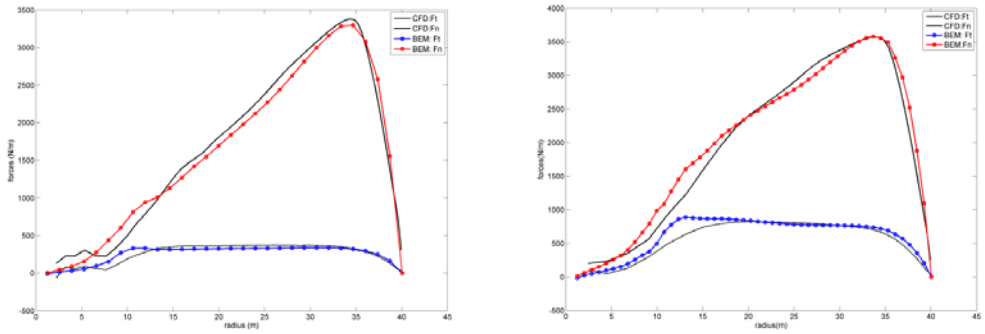

Figure 58: Simulated forces along blade for the 3MW wind turbine at wind speed of 10m/s (left) and 15m/s (right)

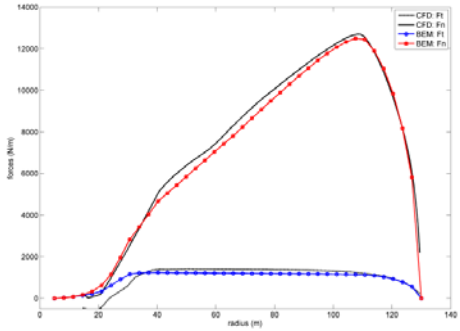

Figure 59: Simulated forces along blade for the 20MW wind turbine at wind speed of 10m/s

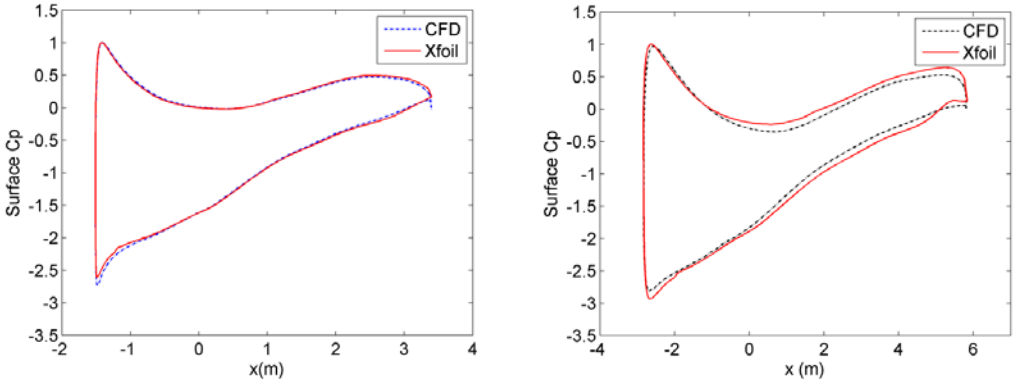

Figure 60: Surface pressure coefficients computed from CFD and Xfoil at Y=80 m (left) and Y=40 m (right)

1.5.9 Development of LM Wind Power acoustic prediction tools

For LM the NextRotor project was aimed at designing low noise blade designs and noise reduction devices like serrations for LM by developing reliable tools for acoustic prediction and testing of designs in anechoic wind tunnels in partnership with DTU.

Tools for acoustic prediction

LM developed robust tools for airfoil noise prediction (LM Airfoil Noise) rotor noise prediction (LM Acoustic suite) & design of serrations for noise reduction (Serration Designer). These tools are semi empirical in nature and they were validated with data from both wind tunnel and field tests.

LM Airfoil Noise tool predicts the far field noise spectra of any airfoil in uniform flow. Figure 61 gives a comparison between experimental data, DTU prediction and LM prediction. LM lmfoil/tno agrees reasonably well with experiment and DTU noise prediction.

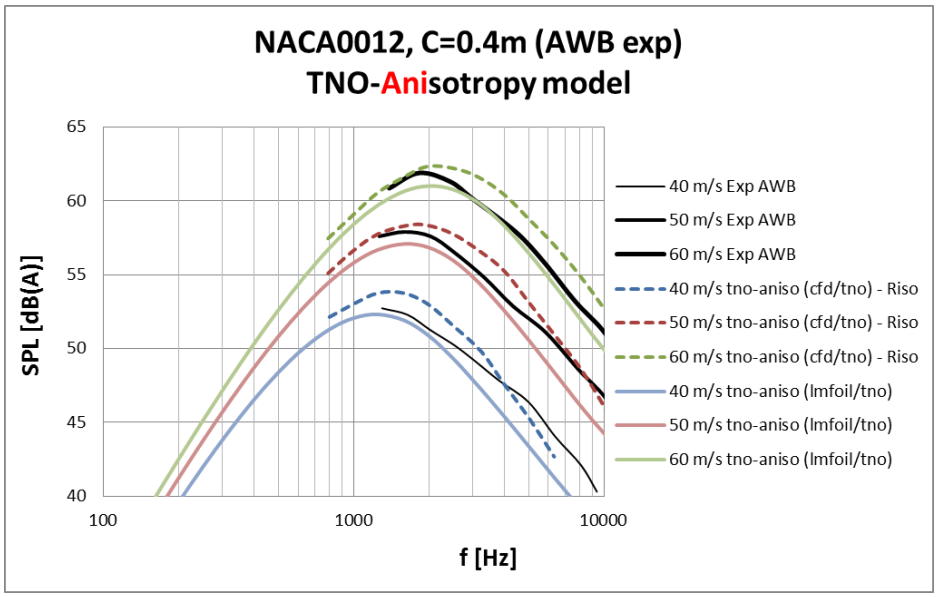

Figure 611: Comparison of experimental data (AWB), DTU noise prediction (cfd/tno), and LM noise prediction (lmfoil/tno)

The LM rotor noise prediction code is capable of giving far field noise predictions of aerodynamically generated wind turbine noise with an accuracy of ±2 dB. Figure 62 shows an example of the validation of the LM rotor noise prediction.

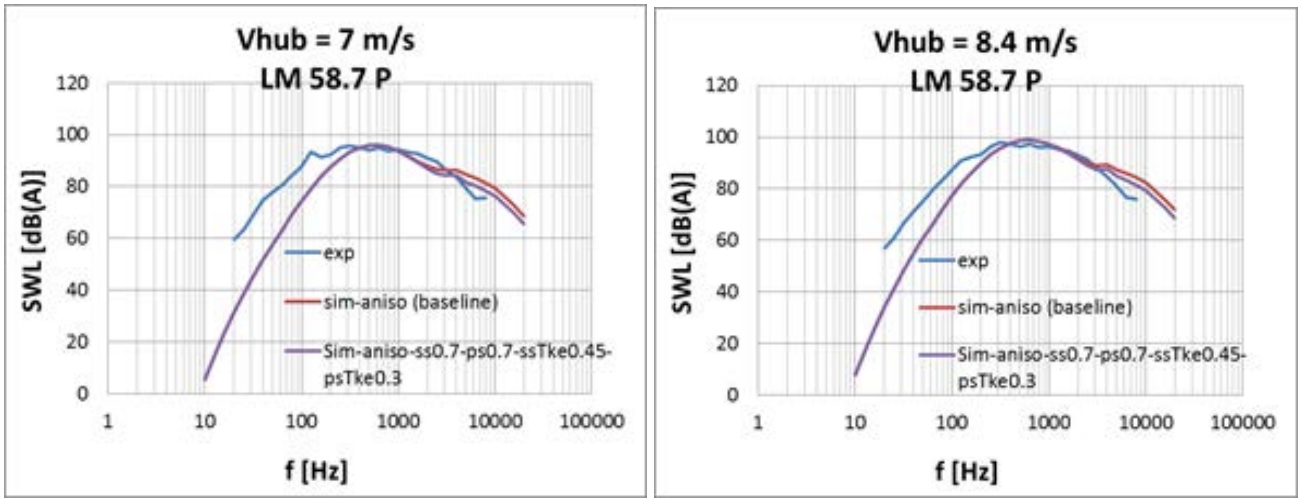

Figure 22: Comparison of experimental data and LM prediction of rotor noise

The Serration Designer tool generates optimized serration designs for any LM blade and turbine operating conditions within ~ 30 mins. Figure 63 shows an example of output from the tool.

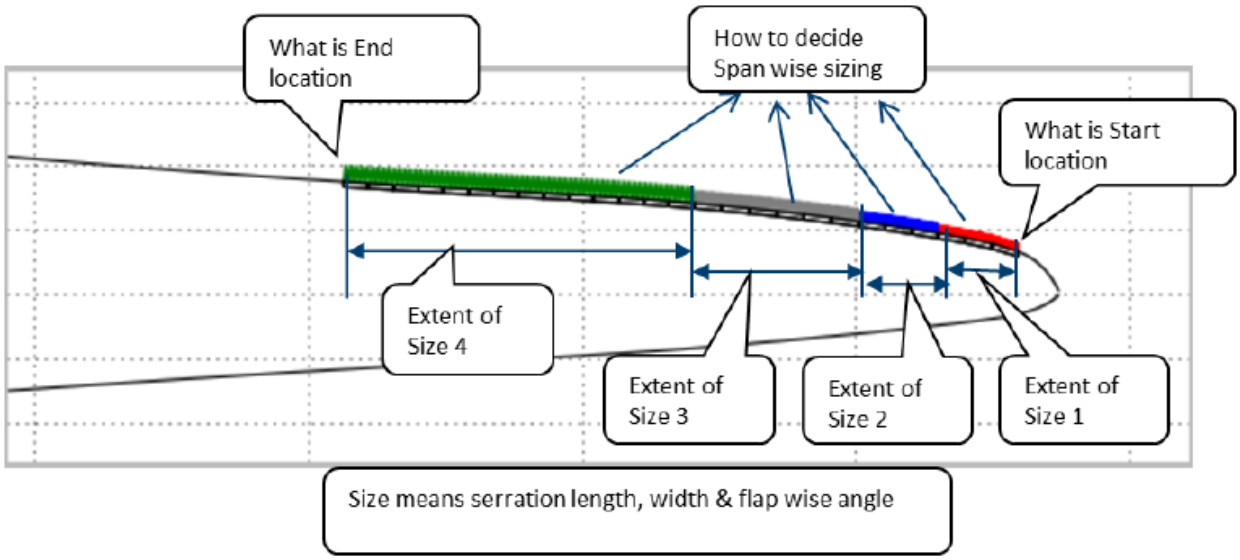

Figure 63: Output from Serration Designer tool

These tools have raised the credibility of LM in the domain of wind turbine noise and enables robust design of low noise blades and noise reduction devices like serrations. The serrations designed by LM were tested in the Virginia Tech anechoic wind tunnel where noise reduction benefit was demonstrated.

Project milestones M5 and CM2

According to the original project plan and budget, a major task deliverable from LM was the retrofitting of the LM LSWT Wind Tunnel into a noise measurement facility. During 2013 LM have been investigating options for doing noise measurements in the existing wind tunnel setup. As part of this work LM also have received help from an external consultant, LMS Engineering (Belgium).

Before making decisions, a feasibility study was carried out with two overall parts: 1) Definition of requirements to a noise measurement facility, and 2) Possibility to measure noise in LSWT to match requirements and estimation of what modifications and installations that would require.

Requirements to a noise measurement facility were derived from the need to compare differences between airfoils and effects of noise reduction devices. Furthermore, these differences should be available for conditions similar or scalable to a full size wind turbine rotor.

A feasibility study was also done in LM wind tunnel for making acoustic measurements from airfoils. In the LM wind tunnel setup with a closed test section (with hard walls) and closed circuit airline, background noise is the main problem. Often wind tunnel background noise can be much louder than noise generated by an airfoil. Experience from other wind tunnels and available research and literature confirms this. Advanced measurement techniques and noise reduction treatments can improve the signal-to-noise ratio. As a consequence, the critical part of the LM feasibility study was to understand the background noise levels and sources in the LM wind tunnel. For this specific task LMS Engineering did a detailed evaluation of background noise in the LM wind tunnel. Some overall conclusions from the LMS report “LM Wind Power Feasibility tests Signal analysis and conclusions” were:

- Airfoil noise is only 3 dB higher than background noise (around 10 dB difference is required).
- Noise measurements are only capable of capturing very loud noise problems on an airfoil, i.e. not meting LM requirements.
- Noise source identification using an advanced beam forming analysis will not be straightforward.
- There is potential for improvement of background noise in the LM wind tunnel.
- Many background noise sources were identified which would require treatment.
- Low frequency noise (required for wind turbines) will be extremely difficult to measure.

Based on the results from the background noise measurement LM did further analysis of possibilities of upgrading the LM wind tunnel. The overall outcome was that a lot of modifications to the existing testing facility would be needed. However, even after doing these modifications there would be no guarantee of meeting the requirements and furthermore current aerodynamic testing capabilities might deteriorate. The required investment was estimated to around 10,000,000dkr.

The LM management decided not to go for this option for retrofitting the LM Wind Tunnel into an acoustic measurement facility. Instead LM will follow another strategy:

1. Use external wind tunnels for acoustic tests, e.g. Virginia Tech. or the coming Danish National Wind Tunnel.
2. Instead of doing direct acoustic measurements in the LM Wind Tunnel, apply advanced flow measurement techniques to characterize flow and turbulence behaviour. Some acoustic properties can be derived from knowledge about flow properties, although such correlations still has to be improved.

Advanced flow measurement systems

Implementation of advanced flow measurement systems were split into two parts:

1. Implementation of robust flow measurement devices in everyday wind tunnel testing (started Q4 2014). Two 5-hole probes have been purchased and implemented in the LM wind tunnel measurement setup. Internship project will focus on applications of the instrumentation (August – December 2015).
2. Implementation of flow measurement devices for special testing purposes (not yet started).

1.5.10 Commercial results

Since the development of noise prediction tools, LM has had several requests from customers for the evaluation of noise from rotors. LM has successfully supported multiple customers in making noise predictions for several turbines carrying LM blades. The tools in addition to predicting the overall noise power levels also predict the detailed acoustic spectra in the field. This aspect has been used in acoustic data diagnostic efforts in the field. The knowledge gained during the course of the NextRotor project has helped LM mature its serration product design and currently LM is able to offer designs that are structurally robust in addition to providing aero and acoustic benefit.

Activities of the Next Rotor project have added tremendous value to LM in terms of developing a better understanding of wind turbine acoustics. Tools developed helps in making better acoustic predictions for rotors. Specifically LM was able to achieve the following from the NextRotor project:

- Design of low noise airfoils

- Design of low noise blades
- Design of serrations for achieving noise reduction targets

Activities of the NextRotor have resulted in an increased number of blade projects with existing and new customers. Over time these blade projects will result in increased employment, exports and turnover for LM. Furthermore, serration offerings as add-on devices have already become a new business area for LM.

1.5.11 Dissemination

The dissemination of results is mainly the publications in international journals and conferences which are listed below:

Journal Publications:

1. J Chen, J Cheng, WZ Shen, "Research on Design Methods and Aerodynamics Performance of CQU-DTU-B21 Airfoil", Advanced Materials Research 2012, vol. 455: 1486-1490.
2. J Cheng, J Chen, WZ Shen, WJ Zhu, X Wang, “Optimization design of airfoil profiles based on the noise of wind turbines”, Acta Energiae Solaris Sinica 2012, vol. 33(4): 558-563.
3. IV Naumov, VV Rahmanov, VL Okulov, CM Velte, KE Meyer, RF Mikkelsen, “Flow diagnostics downstream of a tribladed rotor model”, Thermophysics and Aeromechanics 2012, vol. 19(2): 171-181
4. CM Velte, VL Okulov, IV Naumov, “Regimes of Flow Past a Vortex Generator”, Technical Physics Letters 2012, vol. 38(4): 379–382, http://link.springer.com/article/10.1134/S1063785012040281.
5. J Chen, J Cheng, WZ Shen, WJ Zhu, X Wang, “Research on improved design of airfoil profiles based on the continuity of airfoil surface curvature of wind turbines”, Acta Energiae Solaris Sinica 2013, vol. 34(4): 547-554.
6. J Chen, Q Wang, WZ Shen, X Pang, S Li, X Guo, “Structural optimization study of composite wind turbine blade”, Materials & Design 2013, Vol. 46, pp. 247-255, http://www.sciencedirect.com/science/article/pii/S0261306912007340.
7. R Garcia, JN Sørensen, WZ Shen, “Three-Dimensional Viscous-Inviscid Coupling Method for Wind Turbine Computations”, Wind Energy 2014, DOI: 10.1002/we.1821.
8. WZ Shen, WJ Zhu, JN Sørensen, “Study of tip loss corrections using CFD rotor computations”, Journal of Physics 2014, vol. 555, 012094, doi:10.1088/1742-6596/555/1/012094 (10 pages).
9. WZ Shen, WJ Zhu, A Fischer, NR Garcia, J Cheng, J Chen, J Madsen, “Validation of the CQU-DTU-B series of airfoils”, Journal of Physics 2014, vol. 555, 012093, doi:10.1088/1742-6596/555/1/012093 (8 pages).
10. WZ Shen, JN Sørensen, “Editorial”, Renewable Energy 2014, vol. 70: 1-2.
11. R Garcia, JN Sørensen, WZ Shen, “Validation of a three-dimensional viscous-inviscid interactive solver for wind turbine rotors”, Renewable Energy 2014, vol. 70: 78-92.
12. WJ Zhu, WZ Shen, JN Sørensen, “Integrated airfoil and blade design method for large wind turbines”, Renewable Energy 2014, vol. 70: 172-183.
13. JT Cheng, WJ Zhu, A Fischer, NR Garcia, J Madsen, J Chen, WZ Shen, “Design and validation of the high performance and low noise CQU-DTU-LN1 airfoils”, Wind Energy 2014, vol. 17: 1817-1833, DOI: 10.1002/we.1668.
14. NR Garcia, JN Sørensen, WZ Shen, “A strong viscous-inviscid interaction model for rotating airfoils”, Wind Energy 2014, vol. 17: 1957-1982, DOI: 10.1002/we.1677.
15. WZ Shen, I Hrgovan, V Okulov, WJ Zhu, J Madsen, “Design of low noise wind turbine rotors using Betz and Joukowski concepts”, Journal of Physics 2014 DOI: http://dx.doi.org/10.1088/1742-6596/524/1/012131, vol. 524.

16. NR Garcia, JN Sørensen, WZ Shen, “Simulation of the yawed MEXICO rotor using a viscous-inviscid panel method”, Journal of Physics 2014, DOI: http://dx.doi.org/10.1088/1742-6596/524/1/012026, vol. 524.
17. WJ Zhu, WZ Shen, JN Sørensen, "Numerical Investigation of Flow Control Feasibility with a Trailing Edge Flap". Journal of Physics 2014, vol. 524, 012151, 11 pages, doi:10.1088/1742-6596/524/1/012102.
18. VL Okulov, “Testing of rotor vortex theories using Betz optimization”, Doklady Physics 2014, vol. 59(1): 16-20.
19. VL Okulov, “Limit cases for rotor theories with Betz optimization”, Journal of Physics Conference Series 06/2014; 524(1):012129, DOI: 10.1088/1742-6596/524/1/012129.
20. VL Okulov, R Mikkelsen, IV Litvinov, IV Naumov, JN Sørensen, “Capabilities of wind turbines designed by blade elements with momentum and lifting line methods”, submitted in Renewable Energy 2015.
21. J Chen, SL Li, WZ Shen, XF Guo, “Structure Design of Composite Wind Turbine Blade with Aeroelastic Effect”, submitted to Acta Energiae Solaris Sinica 2015.

Conference publications:

1. WJ Zhu, WZ Shen, F Bertagnolio, JN Sørensen, “Comparisons between LES and wind tunnel hot-wire measurements of a NACA0015 airfoil”, Proc. of EWEA2012, Copenhagen, 8 pages, 2012.
2. WZ Shen, MB Montes, PF Odgaard, NK Poulsen, HH Niemann, “Operation design of wind turbines in strong wind conditions”, Proc of EWEA2012, Copenhagen, 10 pages, 2012.
3. VL Okulov, JN Sørensen, “Theories of optimal rotor (oral presentation)”, Proceedings of the 23rd International Congress of Theoretical and Applied Mechanics, 19-24 August, 2012, Beijing, China (Editors: Yilong Bai, Jianxiang Wang, Daining Fang), no- MS01-012.
4. NR Garcia, JN Sørensen, WZ Shen, “Development of a three-dimensional viscous-inviscid coupling method for wind turbine computations”, Proc. 2013 international conference on aerodynamics of offshore wind energy systems and wakes (ICOWES2013), Copenhagen, pp. 69-81.
5. WJ Zhu, WZ Shen, “Integrated airfoil and blade design method for large wind turbines”, Proc. 2013 international conference on aerodynamics of offshore wind energy systems and wakes (ICOWES2013), Copenhagen, pp. 318-326.
6. WZ Shen, “Denmark wind energy programme”, Proc. World Renewable Energy Conference XIII, London, 2014.
7. I Hrgovan, WZ Shen, WJ Zhu, J Madsen, R Hansen, “Design and experimental validation of thick airfoils for large wind turbines”, Proc. World Renewable Energy Conference XIII, London, 2014.
8. NR Garcia, JN Sørensen, WZ Shen, “Hybrid wake model for free vortex viscous-inviscid simulations”, Proc. World Renewable Energy Conference XIII, London, 2014.
9. WJ Zhu, WZ Shen, “Numerical simulation of airfoil trailing edge serration noise”, Proc. Wind Turbine Noise Conference (WTN2015), Glasgow, 2015, 10 pages.

1.5.12 Conclusions

The objectives stated in the project proposal have been realized in a high degree. There are many fruitful results obtained during the project period which have been summarized in Subsections 1.5.1-1.5.10. In conclusion the project has been finished successfully.

References:

[1] JT Cheng, WJ Zhu, A Fischer, NR Garcia, J Madsen, J Chen, WZ Shen, “Design and validation of the high performance and low noise CQU-DTU-LN1 airfoils”, Wind Energy 2014, vol. 17: 1817-1833, DOI: 10.1002/we.1668.

[2] J Hager, S Eyi, K Lee, “Two-point transonic airfoil design using optimization for improved off-design performance”. Journal of Aircraft 1994, 31(5).
[3] WJ Zhu, WZ Shen, “Integrated airfoil and blade design method for large wind turbines,” Proceeedings of the 2013 International Conference on Aerodynamics of Offshore Energy Systems and Wakes, Lyngby, Denmark, pp. 318–326.
[4] I Hrgovan, WZ Shen, WJ Zhu, J Madsen, R Hansen, “Design and experimental validation of thick airfoils for large wind turbines”, Proc. World Renewable Energy Conference XIII, London, 2014.
[5] WJ Devenport, RA Burdisso, A Borgoltz, P Ravetta and MF Barone, “Aerodynamic and acoustic corrections for a Kevlar-walled anechoic wind tunnel”, Proc. of the 16th AIAA/CEAS Aeracoustics Conference, 2010.
[6] TJ Mueller, “Aeroacoustic measurements”, ISBN 3-540-41757-5, Springer-Verlag Berlin Heidelberg New York, 2002.
[7] WZ Shen, WJ Zhu, A Fischer, NR Garcia, J Cheng, J Chen, J Madsen, “Validation of the CQU-DTU-B series of airfoils”, Journal of Physics 2014, vol. 555, 012093, doi:10.1088/1742-6596/555/1/012093 (8 pages).
[8] R Hansen, “LSWT Campaign Report on DTU-LN218”, LM Wind Power, November 2012.
[9] R Hansen, “LSWT Campaign Report on DTU-LN221”, LM Wind Power, November 2012.
[10] R Hansen, “LSWT Campaign Report on DTU-LN224”, LM Wind Power, November 2012.
[11] R Hansen, “LSWT Campaign Report on DTU-230”, LM Wind Power, June 2014.
[12] R Hansen, “LSWT Campaign Report on DTU-236”, LM Wind Power, June 2014.
[13] J Katz, A Plotkin, “Low Speed Aerodynamics: From Wing Theory to Panel Methods”, Second Edition. Cambridge University Press: New York, NY, USA, 2001.
[14] JG Leishman, MJ Bhagwat, A Bagai, “Free-Vortex Filament Methods for the Analysis of Helicopter Rotor Wakes”, Journal of Aircraft 2002, 5: 759–775.
[15] MP Scully, “Computation of Helicopter Rotor Wake Geometry and Its Influence on Rotor Harmonic Airloads”, Ph.D. Thesis, Massachusetts Institute of Technology. Dept. of Aeronautics and Astronautics, 1975.
[16] HB Squire, “The growth of a vortex in turbulent flow”, Aeronautical Quarterly 1965, 16: 302–306.
[17] MJ Bhagwat, JG Leishman, “Accuracy of Straight-Line Segmentation Applied to Curvilinear Vortex Filaments”, Journal of the American Helicopter Society 2001, 46:2:166-169.
[18] NR Garcia, JN Sørensen, WZ Shen, “A strong viscous-inviscid interaction model for rotating airfoils”, Wind Energy 2014, vol. 17: 1957-1982, DOI: 10.1002/we.1677.
[19] JG Schepers, H Snel, “Model experiments in controlled conditions”, Final Report, The Energy Research Center of the Netherlands, 2007.
[20] J Jonkman, S Butterfield, W Musial, G Scott, “Definition of a 5-MW reference wind turbine for offshore system development”, Technical Report NREL/TP-500-38060, Golden, CO: National Renewable Energy Laboratory, February 2009.
[21] WJ Zhu, WZ Shen, JN Sørensen, “Integrated airfoil and blade design method for large wind turbines”, Renewable Energy 2014, vol. 70: 172-183.
[22] MOL Hansen, “Aerodynamics of Wind Turbines”, Earthscan: London. 2008. P. 181.
[23] Okulov VL, Mikkelsen R, Litvinov IV, Naumov IV, Sørensen JN, “Capabilities of wind turbines designed by blade elements with momentum and lifting line methods”, submitted in Renewable Energy 2015.
[24] A Betz, “Schraubenpropeller mit geringstem Energieverlust: mit einem Zusatz von L. Prandtl”, Göttinger Nachrichten, Göttingen 1919.
[25] MATLAB and Optimization Toolbox Release 2015a, The MathWorks, Inc., Natick, Massachusetts, United States
[26] Bekendtgørelse om støj fra vindmøller (Statutory Order on Noise from Wind Turbines), Bekendtgørelse nr. 1284 af 15, december 2011 (Danish Ministry of the Environment, 2006).
[27] T Brooks, D Pope, and M Marceline, “Airfoil Self-Noise and Prediction”, NASA Reference Publication 1218, National Aeronautics and Space Administration, 1989.

[28] RK Amiet, “Acoustic radiation from an airfoil in a turbulent stream”, Journal of Sound and Vibration 1975, 41(4), pp.407–420.
[29] X Wang, WZ Shen, W Zhu, JN Sørensen and J Chen, “Shape optimization of wind turbine blades”, Wind Energy 2009, Vol. 12, pp. 781-803.
[30] NWTC Information Portal (PreComp). https://nwtc.nrel.gov/PreComp. Last modified 30-September-2014 ; Accessed 18-June-2015

1.6 Utilization of project results

DTU Wind Energy is the coordinator of the actual EUDP project. As DTU is a university, the results obtained in the project, especially the new design tools and new computational methods are considered as the state-of-the-art in low noise wind turbine design and will be further used for future researches or projects in the same area. Moreover, some developed computational tools can also be used to analyse the performance of wind energy systems.

LM is the industrial partner of the project. The NextRotor project has given a boost to acoustics activities at LM Wind Power. We are currently recognized as one of the leaders in the market that develop low noise blades and noise reduction devices. Next steps for further commercialization are:

Tools for acoustic prediction:

Since roll out of tools in 2011/2012 they are being used in daily work to support LM customers and the tools have in several cases helped to ensure orders for both new blade designs and for increased volume of existing designs. Tools are continuously being validated against experimental data and further developed.

Low noise airfoil design:

LM does not have specific ”Low-Noise” airfoils. However, acoustics is considered for any new airfoil design to meet optimum performance.

Low noise blade design:

All new (on-shore) LM blade designs are evaluated for noise. A few blades have been designed specifically for low noise. LM expects further interest from customers (also outside Europe) in the future.

Serration devices for noise reduction:

Development was not a part of NextRotor, but prediction tools and acoustic understanding are utilized. First generation of LM serrations have been sold since 2014. Second generation is currently being rolled out. LM expects an increasing need for such technologies. Further development, validation and commercialization are planned.

1.7 Project conclusion and perspective

The project has been finished successfully. The main results include the new high performance low-noise airfoils and its experimental validations, the development of new design tools for both airfoils and rotors, the development of new computational tools for rotor performance analysis, and the use of the obtained results into commercial products, which have been described briefly in Subsections 1.5.1-1.5.10.

As the current project mainly focuses on the design of highly efficient and low noise wind turbine airfoils and blades, the future focus will be the development of low noise control techniques, such as trailing edge serrations including its performance, modelling and design. These control techniques will be used for further reduction of noise generated from wind turbines.

For LM, as a wind turbine blade manufacturer, involved in some of the world’s most ambitious wind projects, it was of cornerstone importance to develop the capability to predict the noise of new blade designs, espe-

cially where highly restrictive noise regulations exist. LM undertook this challenge under the NextRotor project and from the ground up built a suite of computational tools that today form the backbone of LM's aeroacoustic capabilities and have become the go-to solution when communication of acoustic information with our customers is needed.

Continued engagement in projects like NextRotor with strategic partners is required to maintain our lead and to raise the bar set on low noise offerings.

Annex

Links are added to the publications listed in Subsection 1.5.10.